

Gemini GMOS/IFU spectroscopy of NGC 1569 – I. Mapping the properties of a young star cluster and its environment

M. S. Westmoquette,¹* K. M. Exter,²*† L. J. Smith^{1,3} and J. S. Gallagher III⁴

¹*Department of Physics and Astronomy, University College London, Gower Street, London WC1E 6BT*

²*Instituto de Astrofísica de Canarias, C/Vía Lactea s/n, E38200 La Laguna, Tenerife, Spain*

³*Space Telescope Science Institute and European Space Agency, 3700 San Martin Drive, Baltimore, MD 21218, USA*

⁴*Department of Astronomy, University of Wisconsin-Madison, 5534 Sterling, 475 North Charter Street, Madison, WI 53706, USA*

Accepted 2007 August 3. Received 2007 July 12; in original form 2007 May 31

ABSTRACT

We present Gemini-North GMOS/IFU observations of a young star cluster and its environment near the centre of the dwarf irregular starburst galaxy NGC 1569. This forms part of a larger and ongoing study of the formation and collimation mechanisms of galactic winds, including three additional IFU pointings in NGC 1569 covering the base of the galactic wind which are analysed in a companion paper. The good spatial and spectral resolution of these GMOS/IFU observations, covering 4740–6860 Å, allow us to probe the interactions between clusters and their environments on small scales. For cluster 10, we combine the GMOS spectrum with *Hubble Space Telescope* imaging to derive its properties. We find that it is composed of two very close components with ages of 5–7 Myr and ≤ 5 Myr, and a combined mass of $7 \pm 5 \times 10^3 M_{\odot}$. A strong red Wolf–Rayet emission feature confirms our young derived cluster ages.

A detailed analysis of the H α emission-line profile shapes across the whole field of view shows them to be composed of a bright narrow feature [intrinsic full width at half-maximum (FWHM) $\sim 50 \text{ km s}^{-1}$] superimposed on a fainter broad component (FWHM $\leq 300 \text{ km s}^{-1}$). By mapping the properties of each individual component, we investigate the small-scale structure and properties of the ionized interstellar medium, including reddening, excitation and electron densities, and for the first time find spatial correlations between the line component properties. We discuss in detail the possible mechanisms that could give rise to the two components and these correlations, and conclude that the most likely explanation for the broad emission is that it is produced in a turbulent mixing layer on the surface of the cool gas clumps embedded within the hot, fast-flowing cluster winds. We discuss implications for the mass-loading of the flow under these circumstances. The average radial velocity difference between the narrow and broad components is small compared to the linewidths, implying that within the IFU field of view, turbulent motions dominate over large-scale bulk motions. We are therefore sampling well within the outer bounding shocks of the expanding superbubbles and within the outflow ‘energy injection zone’.

Key words: ISM: kinematics and dynamics – galaxies: evolution – galaxies: individual: NGC 1569 – galaxies: ISM – galaxies: starburst.

1 INTRODUCTION

This is the first in a series of papers presenting Integral Field Unit (IFU) observations of ionized gas in the dwarf starburst galaxy NGC

1569. The study is aimed at examining the small-scale relationship between the interstellar medium (ISM) and star cluster population. In this paper we focus on the data reduction techniques and present the first results.

At a distance of $2.2 \pm 0.6 \text{ Mpc}$ (Israel 1988), NGC 1569 is one of the closest examples of a starburst and an excellent analogue to high-redshift dwarf starbursts implicated in theories of galaxy formation. The total *B* magnitude of NGC 1569, $M_B = -17$ (Israel 1988), and a remarkably homogeneous metallicity of $0.25 Z_{\odot}$ (Devost, Roy

*E-mail: msw@star.ucl.ac.uk (MSW); kexter@stsci.edu (KME)

†Present address: Space Telescope Science Institute, 3700 San Martin Drive, Baltimore, MD 21218, USA.

& Drissen 1997; Kobulnicky & Skillman 1997) makes this galaxy similar (in some ways) to the Small Magellanic Cloud.

NGC 1569 has attracted considerable attention because observations at a variety of wavelengths show that it has recently undergone a galaxy-wide burst of star formation that peaked between 100 and 5–10 Myr ago (Greggio et al. 1998). The presence of numerous H II regions reveals that there is still substantial ongoing star formation (Waller 1991). The two well-known superstar clusters (SSCs) A and B (Ables 1971; Arp & Sandage 1985) are prominent products of the starburst episode, which may have been triggered by an interaction with a nearby H I cloud (Stil & Israel 1998; Mühle et al. 2005). An extended system of H α filaments, indicative of a bipolar outflow is seen (Heckman et al. 1995; Martin 1998). X-ray observations show that the wind is metal-enriched and emanates from the full extent of the H α disc (Martin, Kobulnicky & Heckman 2002), but only from ~ 0.6 times the extent of the H I disc (Waller 1991; Martin et al. 2002; Stil & Israel 2002, their fig. 7).

The star cluster population of NGC 1569 has been studied extensively using *Hubble Space Telescope* (HST) observations. Hunter et al. (2000) identified and catalogued a total of 48 compact but resolved clusters using WFPC2 imaging. Using the same data but different criteria, Anders et al. (2004) found 179 clusters, with the majority being formed in an intense starburst event which began ~ 25 Myr ago. Of the cluster population, only the most luminous clusters A, B and no. 30 (nomenclature from Hunter et al. 2000) have been studied in any detail. These three SSCs alone provide a significant fraction (20–25 per cent) of the total optical and near-infrared (near-IR) light in the central region of NGC 1569 (Origlia et al. 2001). Cluster A has actually been resolved into two clusters (de Marchi et al. 1997), and has an integrated age of ~ 7 Myr, with a probable small age difference between the two components (Hunter et al. 2000; Maoz, Ho & Sternberg 2001; Origlia et al. 2001). Clusters B and 30 are older with ages of 10–20 and ~ 30 –50 Myr, respectively (Hunter et al. 2000; Origlia et al. 2001; Anders et al. 2004).

The most conspicuous active star-forming region is located 90 pc to the west of cluster A and corresponds to the brightest H II region in NGC 1569 (no. 2; Waller 1991), and the peak of the thermal radio emission (Lisenfeld et al. 2004), the dust emission (Lisenfeld et al. 2002) and the submillimetre/far-IR emission (Galliano et al. 2003). This region is at the eastern edge of a large CO cloud complex (Taylor et al. 1999), which contains and is surrounded by a number of radio continuum sources (Greve et al. 2002). Hunter et al. (2000) find two clusters in this region, numbers 6 and 10, the latter of which is found by Tokura et al. (2006) to be surrounded on one side by mid-IR [S IV]10.5 μ m emission coincident with a gas knot clearly visible in H α . Cluster 10, one of the subjects of this paper, is the third visually brightest cluster after A and B (Hunter et al. 2000), but has not been studied in any detail thus far.

Stellar wind and supernova-driven outflows powered by the collective injection of kinetic energy and momentum from massive stars in starbursts can drastically affect the structure and subsequent evolution of dwarf galaxies. In NGC 1569, H α images show a chaotic, complex, ionized structure with filaments, bubbles and loops (Hunter, Hawley & Gallagher 1993; Tomita, Ohta & Saito 1994; Heckman et al. 1995; Anders et al. 2004) while the neutral ISM is highly turbulent (Stil & Israel 2002). Heckman et al. (1995) observe H α line profiles which are ‘distinctly non-Gaussian’, exhibiting broad, asymmetric wings that they decompose using multi-Gaussian profile fitting. Within 2 arcsec of SSC A, the H α line has a full-width zero-intensity of 30–50 Å and they find the wings to account for up to ~ 30 per cent of the total H α flux within this region.

Broad emission-line wings have been detected in many giant H II regions both in nearby galaxies (30 Dor: Chu & Kennicutt 1994; Melnick, Tenorio-Tagle & Terlevich 1999; NGC 604: Yang et al. 1996; NGC 2363: Roy et al. 1992, González-Delgado et al. 1994) and in more distant dwarf galaxies (Marlowe et al. 1995; Izotov et al. 1996; Homeier & Gallagher 1999; Sidoli, Smith & Crowther 2006). Westmoquette et al. (2007b) present high-resolution HST/STIS observations of the central regions of M82, and identify a ubiquitous underlying broad component to the optical nebular emission lines in this galaxy. They were able to track the properties of this component through the central starburst regions, and relate them to the highly fragmented state of the ISM.

The nature of the energy source for these broad lines is not clear, and a number of contesting explanations have been proposed, all of which relate to the action of stellar winds and supernovae (SNe): broad lines resulting from the hot, turbulent gas confined to large bubbles blown by the winds; large velocities associated with supernova remnants (SNRs); integrating over many ionized structures (shells) with different expansion velocities; or from blow-out phenomena such as champagne flows or superwinds. These mechanisms act to differing degrees over differing spatial extents depending on the ambient physical conditions; the linewidths and integrated shapes thus change accordingly. This makes an assessment of their effect or importance difficult, particularly since the available observations are often conflicting. Through the data presented here, we attempt to clarify which mechanisms could apply in the case of NGC 1569.

HST narrow-band H α images, in particular, illustrate that the ISM contains many small-scale structures (e.g. Buckalew & Kobulnicky 2006). To probe the roots of the wind outflow from NGC 1569, it is necessary to investigate the interaction of the individual winds from clusters with their environments on high angular scales. Good spectral resolution and spatial coverage are, however, equally important for determining properties such as gas dynamics and excitation mechanisms. Integral field spectroscopy (IFS) is ideally suited to these type of observations, and modern, large format IFUs, such as those found on 8-m class telescopes, currently provide the best opportunity to fulfil these demanding requirements. Historically, it has been very difficult to manage the data products from such instruments, but in recent years the infrastructure to deal with the reduction, analysis and visualization of IFS data has improved dramatically.

To this end we have obtained Gemini-North GMOS/IFU observations of the cluster wind–ISM interaction zone in the central region of NGC 1569. Our observations focus on the small-scale and are of high enough spatial resolution to study the wind–ISM interaction processes in detail. In this first paper we present the data set for one of four IFU positions, and describe in detail the reduction and analysis techniques employed and the software tools we have developed. In a second paper (Westmoquette et al. 2007a, hereafter Paper II) we present the analysis of the remaining IFU positions covering the central outflow region. In a third paper (Westmoquette et al. 2007; hereafter Paper III) we will examine the properties of the outer wind regions using deep H α imaging and IFU observations.

2 OBSERVATIONS AND DATA REDUCTION

2.1 Observations

In 2004 November queue-mode observations using the Gemini-North Multi-Object Spectrograph (GMOS) IFU (Allington-Smith

et al. 2002) were obtained covering four regions near the centre of NGC 1569 (programme ID: GN-2004B-Q-33, PI: L. J. Smith), with 0.5–0.8 arcsec seeing (6–9 pc at the distance of NGC 1569). A nearby bright star was used to provide guiding and tip-tilt corrections using the GMOS on-instrument wavefront sensor.

Depending on the combination of spatial and spectral coverage required, the GMOS IFU can be operated in one- or two-slit modes. For our purposes, we opted for the one-slit mode giving a field of view (FOV) of 5×3.5 arcsec² (which corresponds to approximately 50×35 pc at the distance of NGC 1569) sampled by 500 hexagonal contiguous fibres of 0.2 arcsec diameter. An additional block of 250 fibres (covering 2.5×1.7 arcsec²) are offset by 1 arcmin from the object field providing a dedicated sky view. The coordinates of the IFU field centre analysed in this paper were $\alpha = 04^{\text{h}}30^{\text{m}}47^{\text{s}}.27$; $\delta = +64^{\circ}51'03''.2$ (J2000) and the total exposure time, split into four separate integrations, was 6720 s. Using the R831 grating to give a spectral coverage of 4740–6860 Å and a dispersion of 0.34 Å pix^{-1} , we were able to cover the important nebular diagnostic lines of H α , H β , [O III] $\lambda\lambda 4959, 5007$, [N II] $\lambda\lambda 6548, 6583$ and [S II] $\lambda\lambda 6716, 6731$.

The GMOS spectrograph is fed by optical fibres from the IFU which reformats the arrangement of the spectra for imaging by the detector. This is composed of three 2048×4068 CCD chips separated by small gaps. In order to remove the pixel-to-pixel sensitivity differences, and enable the wavelength and flux calibration of the data, a number of bias frames, flat-fields, twilight flats, arc calibration frames and observations of the photometric standard star G191-B2B were taken contemporaneously with the science fields.

The IFU positions were chosen to cover selected areas of the disturbed ionized ISM in the inner region of NGC 1569, near the roots of the wind outflow. In this paper we present data for one position which samples cluster 10 and its immediate environment. In Fig. 1, we show the position of the IFU field on an archive *HST* F656N image (GO 6423, PID. Hunter; see Table 1) obtained with the Wide Field Planetary Camera 2 (WFPC2). Cluster 10 is located on the easternmost part of the ionized complex centred on H II region 2 (Waller 1991) and is ideal for the study of the cluster–ISM interaction. Just off the south-west edge of the IFU field are two tentative 1.44-MHz detections M-c and M-d of Greve et al. (2002). To the

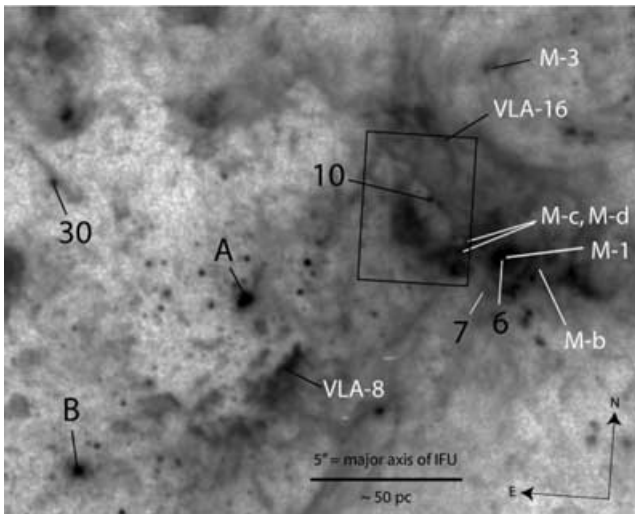


Figure 1. *HST*/WFPC2 image taken through the F656N filter of the central region of NGC 1569 showing the position of the IFU field. A number of the most prominent star clusters (Hunter et al. 2000) and radio continuum sources (Greve et al. 2002) are labelled in black and white, respectively.

north of the field, ~ 25 pc from cluster 10, is VLA-16, a non-thermal radio source also reported by Greve et al. (2002) who consider it may be an extended low surface brightness SNR.

2.2 Data reduction

Because of the complexity of the data products from IFU instruments, a considerable amount of time was invested in learning and developing reduction and analysis tools to enable us to extract the most information we could from this extensive data set.

The field-to-slit mapping for the GMOS IFU reformats the layout of the fibres on the sky to one long row containing five blocks of 100 object fibres interspersed by five blocks of 50 sky fibres. In this way, all 750 spectra can be recorded on the detector at the same time.

Basic reduction was performed using the Gemini pipeline reduction package (implemented in IRAF¹). There are a number of tasks within this package that are designed to perform certain functions, and each contains switches to allow them to be applied at different stages of the reduction procedure. The first stage was to run the *gfreduce* task on the flat-fields, twilight flats and arc calibration exposures in order to prepare the raw files for reduction, and subtract the overscan level and bias frames. *gfextract* traces and extracts the spectrum of each fibre (using a ± 2.5 pixel aperture in the spatial direction), and by running this on the flat-field image, produces a reliable trace of the position of each spectrum on the CCD. We then ran *gfresponse* on the *gfreduce*'d twilight flats to create a throughput correction function for each fibre (an essential step to correct differences in fibre-to-fibre transmission). The final step before reducing the science data was to extract the 750 arc calibration spectra from the arc lamp exposures (using *gfreduce*) and establish and apply a wavelength calibration solution using *gswavelength* and *gtransform*.

Running *gfreduce* on the science observations using the spectrum trace created from the flat-field, the throughput correction determined from the twilight flat, and the wavelength calibration from the arc exposures, creates a data file containing 750 reduced spectra, each one pixel in width and ordered by the position they were recorded on the CCD (which we will call the 'fibre order'). After extraction of the spectra, the x and y spatial unit is now termed 'spaxel' to differentiate from 'pixel' which refers to the CCD.

Cosmic rays were cleaned from the data at this stage with the Laplacian cosmic ray identification routine *lacosmic* (van Dokkum 2001). Fits to the flux of the [O I] $\lambda 5577$ telluric emission line, assumed to remain spatially stable in intensity for each observation set, for each of the 750-object spectra, showed a significant (~ 10 per cent) dip from the centre to the edges when plotted against fibre order. We decided that a second throughput correction was needed to remove this variation. This correction was measured by fitting a fourth-order polynomial to the intensity curve, inverting the profile, normalizing it to unity, then dividing this into the data using the IRAF task *imarith*.

Fits to the full width at half-maximum (FWHM) of the [O I] $\lambda 5577$ line also showed unexpected variations with fibre order. We found that the groups of 50 sky fibres at either end of the CCD showed elevated widths compared to the central groups. Thus to be safe we extracted only sky fibres in the central blocks (i.e. fibres 200–250,

¹ The Image Reduction and Analysis Facility (IRAF) is distributed by the National Optical Astronomy Observatories which is operated by the Association of Universities for Research in Astronomy, Inc. under cooperative agreement with the National Science Foundation.

Table 1. *HST* archive images of NGC 1569.

Filter	Camera/CCD	Plate scale (arcsec pix ⁻¹)	Exposure time (s)	Programme ID	PI
F330W	ACS/HRC	0.026	220 × 3	9300	H. Ford
F439W	WFPC2/PC	0.045	700 × 16	6111	C. Leitherer
F555W	ACS/HRC	0.026	130 × 3	9300	H. Ford
F656N	WFPC2/PC	0.045	800 × 2	6423	D. Hunter
F814W	ACS/HRC	0.026	130 × 3	9300	H. Ford

350–400 and 500–550). After extracting and averaging these fibres for each science frame, the resulting spectrum was subtracted from the rest of the spectra using imarith. Because of diffuse emission from the galaxy extending past the 1 arcmin separation of the object and sky fields, there is the possibility that nebular emission could contaminate the sky spectra. To check the level of such contamination, we compared the flux of the H α line in representative spectra with and without sky subtraction. The difference in the flux for each case was 1–2 per cent and therefore deemed insignificant.

2.3 Flux calibration

As part of the calibration data set, the flux standard star G191-B2B (Oke 1990) was observed using the same instrument set-up as described in Section 2.2. Reduction of these data followed the same procedure as described above for the science frames, except that we used the throughput response file and wavelength solution determined from the reduction of one of the other IFU fields. In order to obtain the optimum signal-to-noise ratio (S/N) spectrum for the standard star, we summed all object spaxels across the FOV using gfapsum to create one averaged spectrum of the standard star. The sensitivity function was computed using the gsstandard task (which includes a second-order extinction correction relevant to the Gemini-North observatory), and the flux calibration for each science frame was performed by the gscalibrate task.

Final combination of the individual exposures for each position was done using imcombine. The resulting data file was then formed of 750 reduced, sky-subtracted and flux-calibrated spectra, one corresponding to each spaxel in the FOV (including the sky field). Separation of the sky fibres from the data files was achieved using the E3D Visualization Tool (Sánchez 2004), the development of which was a primary goal of the European Commission’s Euro3D Research Training Network. Each science file now only contained the 500-object spectra.

In order to determine an accurate measurement of the instrumental contribution to the line broadening, we selected spectral lines from a wavelength calibrated arc exposure that were close to the H α and [O III] λ 5007 lines in wavelength, and sufficiently isolated to avoid blends. We then fitted single Gaussians to these lines for all 750 apertures and took the average. The instrumental broadening (velocity resolution) of the final data set varies between FWHM = 74 ± 5 km s⁻¹ at the blue end (with an average S/N of 4.6 in the continuum) and 59 ± 2 km s⁻¹ at the red end (with an average S/N of 14.5).

2.4 Differential atmospheric refraction correction

When observing the spectrum of an object, its light is refracted by the Earth’s atmosphere by varying amounts at different wavelengths. This effect, termed differential atmospheric refraction (DAR), is

therefore a function of wavelength (horizontal) and airmass (vertical). An advantage of IFS over traditional long-slit methods is that it is possible to determine and correct the effects of DAR using an a posteriori procedure (e.g. Arribas et al. 1999). In order to correct our data for DAR, we first had to convert each data set to standard cube format. This involves changing the way in which the data are stored, from one spectrum (wavelength versus flux) per spaxel (spatial co-ordinate) to a 2D flux image at each wavelength point. For the DAR correction procedure, it is required that the data are sampled evenly in x and y , and since the format of the GMOS fibres is hexagonal we had to apply an interpolation routine to resample the data into contiguous squares with an equivalent ‘diameter’. A diameter of 0.18 arcsec gave the closest match to the *number* of original spaxels when interpolating from hexagons to squares.

Measurement of the DAR shift can be achieved easily and automatically if there is an unresolved point source in the FOV: in our case cluster 10. With the data in cube format (two spatial axes and one of wavelength) and using scripts provided by L. Christensen (ESO), the spatial shifts were traced by cutting the cubes into a series of monochromatic images, and fitting a 2D Gaussian function to the unresolved star cluster to determine the centroid position. A third-order polynomial was used to fit this trace (with wavelength) through the data cubes, giving the relative shifts in right ascension and declination for each slice with respect to the first (reference) wavelength. The measured offsets were then used to shift each wavelength slice by then required amount, and were the combined back into a data cube with the original grid sampling using a modified version of the IRAF STSDAS² drizzle task (originally written as an implementation of the image combination method known as variable-pixel linear reconstruction; Fruchter & Hook 2002). The result is a data cube where every flux at each point in the object corresponds to the same position in the image for each wavelength point.

The final stage was to crop the edges of each field in order to remove spaxels only containing flux for part of the wavelength range. This is an inevitable side effect of performing a DAR correction.

2.5 *HST* images

To supplement our studies, we obtained *HST* ACS/HRC and WFPC2 broad- and narrow-band images of the central regions of NGC 1569 from the *HST* archive. These images are listed in Table 1 (together with the corresponding programme IDs and PI) and were calibrated using the ‘on-the-fly’ pipeline system. Dithered images were first registered using their WCS (World Coordinate System) information, then combined using the IRAF imcombine routine in order to remove cosmic rays.

² STSDAS is the Space Telescope Science Data Analysis System; its tasks are complementary to those in IRAF.

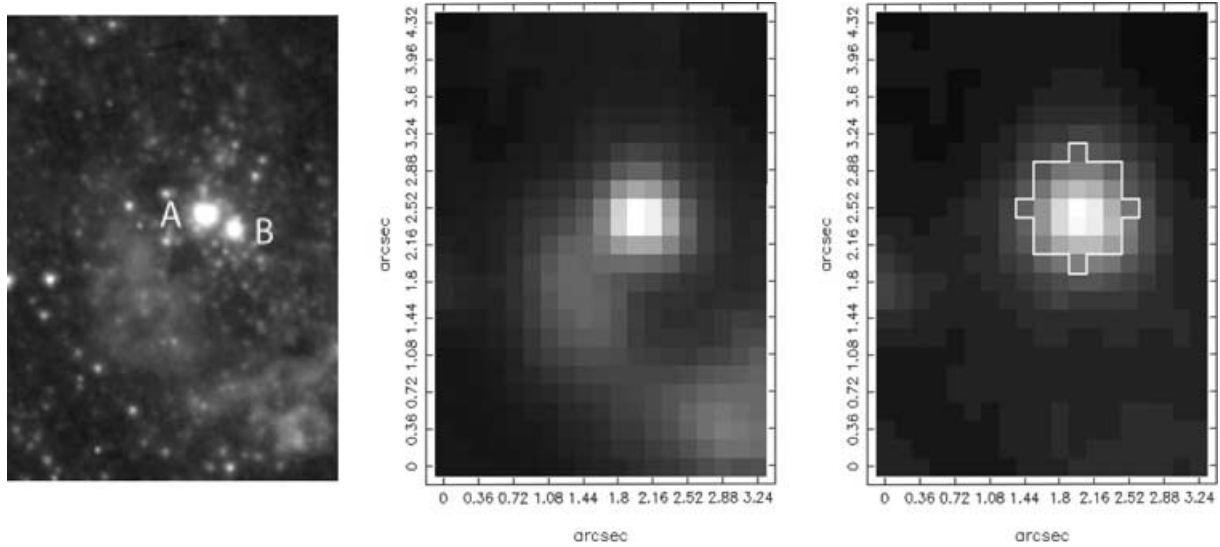


Figure 2. Left-hand panel: *HST*/ACS HRC F555W image of the region covered by the IFU pointing. The two components of cluster 10 are labelled. Central panel: IFU data convolved with a V-band filter function. Right-hand panel: flux map in the continuum only (6645–6660 Å), showing the position of cluster 10 and the spaxels extracted to form the cluster spectrum. North is up and east is towards the left-hand side.

Fig. 2 introduces the concept of imaging with IFU data. On the left-hand panel is the *HST* ACS/HRC F555W image of the region covered in our IFU pointing. In the centre we show a ‘virtual’ V-band image reconstructed from our IFU data by convolving the spectrum from each spaxel with a V-band filter function. The similarity between the two images is obvious once the resolution of each is taken into account (ACS/HRC = 0.026 arcsec pixel^{−1}; GMOS IFU = 0.18 arcsec spaxel^{−1} but seeing-limited at ∼0.8 arcsec). One must keep in mind the fact that the ACS F555W filter contains contamination from nebular [O III] emission, which is why a certain amount of nebulosity is seen surrounding cluster 10. The right-hand plot is of the same field but restricted in wavelength to cover the continuum only (in the range 6645–6660 Å). Overlaid is an outline of the 24 spaxels summed to create a spectrum of cluster 10 (Section 3).

3 CLUSTER 10

Cluster 10 is the third visually brightest cluster identified by Hunter et al. (2000) but, as can be seen from Fig. 2 (left-hand panel), it is in fact a double cluster. Because of the close proximity of the two sources, previous studies (e.g. Hunter et al. 2000) have treated cluster 10 as one object. Fitting the light profiles across the length and breadth of the IFU field with a Gaussian profile yields an average FWHM of 4.7 spaxels or 0.84 arcsec. This corresponds to the maximum seeing disc size at the time of observation, meaning that the two subclusters are not resolved in our IFU data.

From the F555W ACS/HRC image, we measure the separation of the two cluster 10 components as 0.35 arcsec (3.7 pc). The coordinates of the two sources are given in Table 3. Measurement of the size of the two clusters was made on the ACS/HRC F555W image, and was achieved using ISHAPE (Larsen 1999) together with the TINYTIM package (Krist 2004) to correct for the point spread function. Using a circular Moffat function with a power index of 1.5, and a fit radius of 0.2 arcsec gives an effective radius, $R_{\text{eff}} = 1.18 \pm 0.05$ pc for the north-eastern component (hereafter cluster 10A; see Fig. 2, left-hand panel), and $R_{\text{eff}} = 0.88 \pm 0.15$ pc for the south-western component (hereafter cluster 10B). Due to this very small separation, and the crowding of the field around clus-

ter 10 with other fainter sources, standard aperture photometry is not possible (and we cannot measure absolute magnitudes). However, if all that are needed is relative magnitudes, then small-radius aperture photometry is sufficient. Using a radius of 4 pixels for the HRC images (F333W, F555W and F814W) and 2.5 pixels for the WFPC2 image (F439W) and suitable background annuli, we measure (F555W – F814W) = 1.12 and (F330W – F439W) = −0.27 for the cluster 10A, and (F555W – F814W) = 0.42 and (F330W – F439W) = −0.90 for cluster 10B. We note that since the cluster radii are so similar, using the same aperture for both does not introduce significant errors.

Fig. 3 shows the evolutionary path of a $Z = 0.004$ STARBURST99 (SB99; Leitherer et al. 1999) instantaneous burst evolutionary-synthesis model with a standard Kroupa initial mass function (IMF) in $U - B$, $V - I$ colour space, together with the colours that have

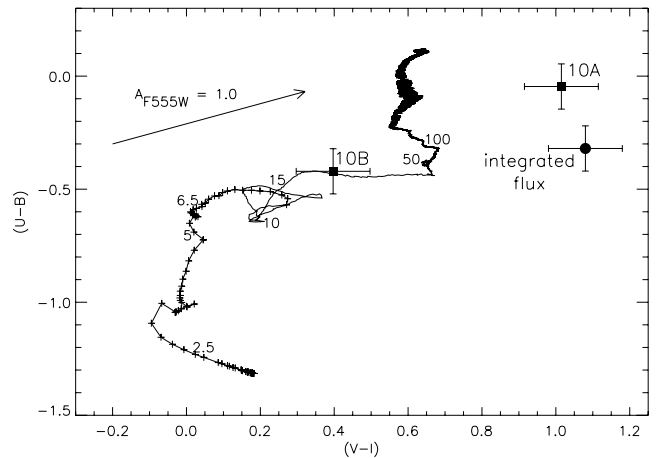


Figure 3. Colour-colour diagram showing (solid line) STARBURST99 instantaneous burst models for $Z = 0.004$. Crosses mark age points on the evolutionary curve from 5–7 Myr; some significant age steps are labelled (units of Myr). The arrow represents the extinction vector for $A_{F555W} = 1.0$. Solid squares show the colours of the two clusters (clusters 10A and 10B); the solid circle shows the colour of the integrated flux of the two.

been determined for both cluster 10 components. Also plotted is the colour of the integrated flux of the two sources (measured using an aperture equivalent in to the cluster size found by Hunter et al. 2000) to compare to parameters derived from the spectrum, since the spectrum is derived from a convolution of the light from both components. SB99 does not give outputs in terms of *HST* filters, so the observed photometry was converted from *HST* to Johnson magnitudes using the conversion factors given by Holtzman et al. (1995) for the WFPC2 data, and Sirianni et al. (2005) for the ACS data. From the diagram we can now derive an approximate age and an estimate of the reddening for each of the cluster components simultaneously. Assuming an extinction value sufficient to deredden each point until it intercepts the model track has the following results. For cluster 10A, an A_V of ≈ 0.8 [$E(B - V) \approx 0.26$] corresponds to an age of 50–100 Myr, whereas $A_V \approx 1.2$ –2 [$E(B - V) \approx 0.65$ –0.40] gives an age of 5–20 Myr. For cluster 10B, zero extinction would imply an age of ~ 20 Myr, an A_V of ≈ 0.3 [$E(B - V) \approx 0.10$] intercepts the track at ~ 7 –15 Myr, whereas an $A_V \approx 0.8$ [$E(B - V) \approx 0.25$] implies an age of ~ 5 Myr. The extinction required for the combined point to cross the track at ~ 5 –7 Myr is $A_V \approx 1.6$ [$E(B - V) \approx 0.54$].

Adopting a Galactic foreground reddening of $A_V = 1.64$ [$E(B - V) = 0.53$] (following Origlia et al. 2001; Relaño et al. 2006), we can immediately rule out ages requiring reddening values less than this. We therefore conclude that 10A must have an age of 5–7 Myr (with a reddening in addition to the Galactic foreground level of $A_V \approx 0.0$ –0.4), and 10B an age of ≤ 5 Myr (consistent with zero reddening after foreground correction). For the colour of the combined point to match these age determinations, the reddening value required is consistent with purely Galactic effects.

A further test to obtain an estimate of the cluster age is to compare the equivalent width of the $H\alpha$ emission line to the predictions of evolutionary synthesis models. Since we only have a spectrum of the combined light from both the clusters, we can only put an upper limit on the flux-weighted age. Measuring an equivalent width of $H\alpha = 91 \pm 3$ Å and using the same SB99 model as used above ($Z = 0.004$, Kroupa IMF), this gives an upper limit to the age of ~ 6.5 Myr, and is consistent with the values derived above.

Now we have an estimated age, we can derive an estimate for the mass by comparing the absolute magnitude, M_{F555W} , to evolutionary synthesis models. As mentioned above, we cannot measure an absolute magnitude of the individual subclusters, but using an aperture large enough to include both, we find a combined $M_{F555W, \text{cluster10}} = -9.61$ mag. Converting to Johnson magnitudes, we find $M_{V, \text{cluster10}} \approx -9.2$ mag, and comparing our measurements to a SB99 6 Myr, $1 \times 10^6 M_\odot$ model results in a predicted mass of 2 – $5 \times 10^3 M_\odot$ (depending on the IMF formulation used) for the combined mass of both subclusters. Since there are uncertainties involved in transforming from the *HST* to Johnson magnitude system, we compared our measured M_{F555W} to the absolute magnitudes predicted by the equivalent Bruzual & Charlot (2003) model (for which results in *HST* filters are given). The derived mass is 7 – $13 \times 10^3 M_\odot$ (depending on IMF), which is in general agreement with the SB99 result. We therefore adopt the value of $7 \pm 5 \times 10^3 M_\odot$ for the combined mass of the two subclusters, meaning that neither of them can be defined as an SSC in the generally accepted definition.

Buckalew et al. (2000) conducted a study of NGC 1569 using *HST* WFPC2 narrow-band imaging of the $\text{He II } \lambda 4686$ line. They discovered fifteen He II emitting sources across the galaxy, of which five were associated with stellar clusters including cluster 10 (specifically only the south-western component; 10B). They attribute the emission as nebular in origin (after Kobulnicky & Skillman 1997, who found widespread nebular He II emission in this region). How-

ever, He II is also strongly emitted in the atmospheres of Wolf–Rayet (WR) stars of both WC and WN type. Buckalew et al. (2000) comment that if the emission they detect in cluster 10 was attributed fully to WR stars, it would correspond to the equivalent of three WNL-type stars (using the calibration of Vacca & Conti 1992). WR stars exist in clusters between ages of approximately 3–5 Myr, so in light of our age estimates for the two cluster components derived above, a WR origin for the He II emission in cluster 10B is perfectly reasonable.

3.1 Cluster spectrum

To extract the spectrum of cluster 10, we summed 29 spaxels (covering an area with an equivalent diameter to the FWHM of the cluster measured from the IFU continuum image) centred on the continuum source as shown on the right-hand plot of Fig. 2. The resulting spectrum is shown in Fig. 4.

The spectrum is dominated by strong emission lines arising from the nebula surrounding the cluster, but also contains a broad emission feature that we identify with $\text{C IV } \lambda\lambda 5801, 5812$ arising from WC-type WR stars. We also detect a large number of weak stellar absorption lines, diffuse interstellar bands (DIBs) and interstellar absorption lines. The detection of a red WR-bump is not unsurprising considering the age we find for cluster 10B, and strengthens the argument for a WR origin for the He II emission detected by Buckalew et al. (2000). Further evidence of the young nature of cluster 10 comes from the high ratio of $[\text{O III}]$ to $\text{H}\beta$ (see Fig. 4, lower line), and the presence of strong $[\text{S III}]$ emission, indicating a high level of ionization in the surrounding H II region, which can only arise in the presence of young O stars.

Simultaneously fitting the WR feature with the superimposed absorption lines, we measure the bump to have an FWHM of ~ 130 Å, a total luminosity of 2.5×10^{37} erg s $^{-1}$ (assuming a distance of 2.2 Mpc and $A_V = 1.64$), and an equivalent width of 12 ± 2 Å. This measured FWHM is unusually broad compared to canonical measurements (Crowther, De Marco & Barlow 1998), and is likely to result from inaccuracies in the fit due to contamination from the superposed DIB absorption lines. Crowther & Hadfield (2006) present measurements of WR bump fluxes for a number of

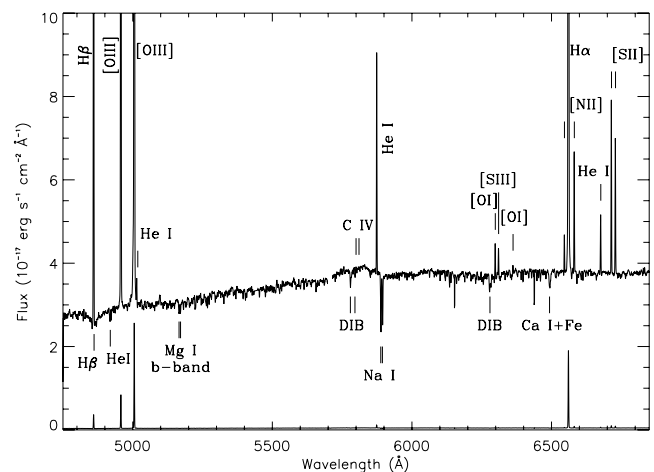


Figure 4. Plot of the extracted spectrum of cluster 10 (smoothed by 5 Å). All identified absorption and emission features are labelled. The lower line corresponds to a $\times 80$ reduction of the main plot to illustrate the spectrum with a full flux range. Notice the strength of the $[\text{O III}] \lambda 5007$ emission compared to the hydrogen recombination lines.

Table 2. Absorption and emission-line measurements for cluster 10 (all lines are emission unless otherwise stated). Widths are corrected for instrumental contribution and velocities are quoted in the heliocentric frame of reference. Typical errors on the velocities of the emission lines are $\sim 5\text{--}10\text{ km s}^{-1}$, and on the widths $\sim 0.5\text{--}5\text{ km s}^{-1}$. Errors for the absorption lines are listed individually.

Line	λ_{air} (Å)	Velocity (km s $^{-1}$)	FWHM (km s $^{-1}$)
H β	4861.33	−84.4	50.7
H β abs ^a	4861.33	−55 ± 40	
He I abs ^a	4921.93	−84 ± 8	
[O III]	4958.92	−79.0	44.7
[O III] ^b	5006.84	−75.1	31.6
He I ^c	5015.68	−74.7	42.3
Mg I abs	5167.32	−77 ± 7	
Mg I abs	5172.68	−89 ± 6	
DIB	5780.5	−40.9 ± 10	160 ± 35
DIB	5797.0	−47.5 ± 20	70 ± 25
He I	5875.67	−82.7	33.9
Na I abs	5889.95	−38 ± 8	
Na I abs	5895.92	−34 ± 8	
DIB	6283.9	−41.0 ± 10	110 ± 20
[O I]	6300.30	−84.9	32.8
[S III]	6312.10	−82.0	50.5
[O I] ^a	6363.78	−80.1	
[N II]	6548.03	−81.4	28.3
H α ^b	6562.82	−89.1	38.8
[N II]	6583.41	−82.8	44.5
He I	6678.15	−81.6	44.1
[S II]	6716.47	−85.1	40.8
[S II]	6730.85	−84.4	46.5

^aLine too weak or confused to measure an accurate FWHM. ^bNarrow component (C1) only. ^cBlended with [O III].

WC4 type stars in the Large Magellanic Cloud (LMC) (the closest galaxy containing a significant population of WR stars at low metallicity $Z = 0.008$) which can be used to determine the equivalent number of stars in our observation. They find one LMC WC4 star to have a red WR-bump luminosity of $3.3 \pm 1.6 \times 10^{36}\text{ erg s}^{-1}$, thus the luminosity equivalent number of WC4 stars in our observed bump is estimated to be 10 ± 5 , once all the uncertainties have been taken into account. For comparison, González-Delgado et al. (1997) find a luminosity equivalent of 20 ± 10 WNL stars in SSC A by measuring the flux in the blue WR-bump.

By fitting Gaussian profiles to all the other emission and absorption lines present in the spectrum, we measured the central velocity and FWHM of each, and present them in Table 2. The average radial velocity of the nebular emission lines is $-82 \pm 4\text{ km s}^{-1}$. Since our cluster spectrum only contains blended photospheric absorption lines, it is not possible to measure an accurate velocity for the stellar component. The evolutionary synthesis models of Bruzual & Charlot (2003) provide a set of spectral energy distributions (SEDs) calculated for similar input ranges as the SB99 models, and although being less accurate at predicting very young ages, their SEDs are derived from actual observed spectral libraries rather than model stellar atmospheres. Their inclusion of observed stellar spectra at high resolution therefore makes them ideal for comparing with our spectrum to derive a cluster velocity. Using a 0.25 Z_{\odot} , 5-Myr instantaneous burst model in the wavelength range 5100–5600 Å (where many faint stellar absorption lines are present), we find a match at $-85 \pm 5\text{ km s}^{-1}$. A good correlation at this velocity is also found at the position of the Ca I + Fe blend at 6494 Å, which is thought

Table 3. Observed and derived properties for cluster 10.

Parameter	Cluster component	
	10A	10B
Adopted systemic velocity (km s $^{-1}$)	−80	
Distance (Mpc)	2.2 ± 0.6^a	
Coordinates (J2000)	04 ^h 30 ^m 47 ^s .16 +64°51′00″.8	04 ^h 30 ^m 47 ^s .12 +64°51′00″.6
(F555W − F814W)	1.12	0.42
(F330W − F439W)	−0.27	−0.90
Half-light radius, R_{eff} (pc)	0.88 ± 0.05	0.60 ± 0.15
Total $E(B - V)$	0.55 ± 0.15	
Electron density, n_e (cm $^{-3}$)	175^{+18}_{-20}	
Age (Myr)	5–7	≤ 5
M_{F555W} (mag)	−9.61	
Mass (M_{\odot})	$7 \pm 5 \times 10^{3b}$	
No. of equivalent WC4 stars	10 ± 5	
Radial velocity (km s $^{-1}$)	−85 ± 5	

^aIsrael (1988). ^bDepending on whether a Salpeter or Kroupa IMF is used.

to be photospheric in origin (Heckman et al. 1995). As well as stellar absorption lines, we detect the interstellar (IS) absorption lines of Na I λ 5890, 5896 and a number of DIBs (Herbig 1995; Heckman & Lehnert 2000). Their velocities are given in Table 2, and are consistent with being Galactic in origin (average velocity $-40 \pm 5\text{ km s}^{-1}$), although the Na I profiles also show blue wings presumably associated with IS absorption within NGC 1569.

Determining the proper heliocentric systemic velocity, v_{sys} , of NGC 1569 has proven to be a difficult task due to its irregular and disturbed morphology. The first study of NGC 1569’s H I gas distribution by Reakes (1980) concluded a $v_{\text{sys}} = -77\text{ km s}^{-1}$. CO observations by Taylor et al. (1999) found the same value, whilst Tomita et al. (1994) and Heckman et al. (1995) found an H α v_{sys} of -90 km s^{-1} and -68 km s^{-1} , respectively, from their long-slit data. A more recent, high-resolution H I study of the NGC 1569 system was made by Mühle et al. (2005), who found the peak of the H I profile at the position of cluster 10 to have a velocity of -80 km s^{-1} (S. Mühle, private communication). Thus, since our measurements of the ionized gas and cluster velocities are also consistent with this value, we adopt a systemic velocity for the cluster 10 region of $v_{\text{sys},10} = -80\text{ km s}^{-1}$.

A check on the value of reddening for the combined light of both cluster components can be made by comparing the observed H α /H β flux ratio with the intrinsic case B values from Hummer & Storey (1987). We derive an absorption-corrected reddening of $E(B - V) = 0.54 \pm 0.15$ mag from Gaussian fits to the H α emission and H β emission and absorption lines. This value is consistent with both the adopted value of Galactic foreground reddening and with the extinctions derived from the colour–colour plot analysis given above. We therefore conclude that cluster 10 only suffers from Galactic foreground reddening, i.e. very little of its light is attenuated by material in NGC 1569 itself. The flux ratio of single Gaussian fits to the [S II] λ 6717, 6731 emission lines gives a value of $1.25^{+0.02}_{-0.01}$ hence an electron density, $n_e = 175^{+18}_{-20}\text{ cm}^{-3}$ (assuming an electron temperature, $T_e = 10^4\text{ K}$). These results are summarized in Table 3.

4 PROPERTIES OF THE IONIZED GAS

We now discuss the IFU data relating to the ionized gas in the environment of cluster 10. The S/N and spectral resolution of these

data are sufficiently high to resolve multiple Gaussian components to each emission line in each of the 500 spectra across the FOV. Before discussing our findings, we first describe the methods used to fit the spectral line profiles and visualize the results.

4.1 Decomposing the line profiles

The automated fitting of multiple profiles to 500 spectra each containing eight emission lines has proved challenging. For this task we have adopted an IDL-based, general-purpose curve-fitting package, called PAN (Peak ANalysis; Dimeo 2005). It was written with the aim of allowing the user to visually interact with the program through the use of IDL's sophisticated 'widget-based' toolkits, and uses the Levenberg–Marquardt technique to solve the least-squares minimization problem. The primary features that caused us to favour this program over any other was its ability to read in multiple spectra at once in an array format, and its method of determining the initial guess parameters of a model profile (namely allowing the user to visually and interactively specify amplitude, position and width). Originally written to analyse data from neutron-scattering experiments, the program has required some modification to suit our needs. We have had to add modules to convert our FITS format data into a format that PAN can read; we have also had to modify the way it outputs the fit results and χ^2 values to something that can easily be read by a plotting package.

To obtain good, reliable fits, the spectra read into PAN had to contain accurate associated error arrays. These error arrays were calculated by taking the square-root of the raw counts in the pre flux-calibrated and throughput-corrected data, converting this to a percentage of the total raw counts, and applying this to the final reduced and calibrated data in order to obtain the uncertainty equivalent to the Poissonian noise. This step was included when converting from FITS to PAN input format. By comparing our error estimates on fits to telluric features (see below) to simple Poissonian statistics, we find this to be a realistic measure of the cumulative uncertainties.

Each line in each of the 500 spectra was fitted using a single, double and triple Gaussian component initial guess, where line fluxes were constrained to be positive and widths to be greater than the instrumental contribution (measured from wavelength calibrated arc exposures to be $74 \pm 5 \text{ km s}^{-1}$ at [O III] and $59 \pm 2 \text{ km s}^{-1}$ at H α ; Section 2.3). The wavelength limits used in fitting each line are given in Table 4. In general, the shape of the emission-line profiles is a convolution of a bright, narrow component overlying a faint, broad component (most obvious in high-S/N lines, e.g. H α). This is consistent with what Heckman et al. (1995) found for the central regions. For the double component fits, the initial guess was always made with the first Gaussian as the narrow component (hereafter referred to as C1), and the second Gaussian as the broader component (hereafter C2). For the triple component fit, the additional component (C3) was specified with an initial guess assigning it to a

supplemental narrow line at the same wavelength as the main narrow line. This consistent approach helped limit the confusion that might arise during analysis as to which Gaussian fit belonged to which component of the line, as well as aiding the χ^2 minimization process.

We used the statistical F -test to determine how many Gaussian components best fit an observed profile. The F -distribution is a ratio of two χ^2 distributions, denoted by the degrees of freedom for the numerator χ^2 and the denominator χ^2 . For statistically comparing the quality of two fits, this function allows one to calculate the significance (χ^2) increase that is associated with a given confidence level, for a given number of degrees of freedom. The test will output the minimal increase of the χ^2 ratio that would be required at the given confidence limit for deciding that the two fits are different. If the χ^2 ratio is higher than this critical value, the fits are considered statistically distinguishable. The output files for the single, double and triple Gaussian models were passed through a script which applied the F -test to extract the results for the most suitable case for each spectral line. Fig. 5 shows two example H α line profiles, each from a different spaxel, with their corresponding Gaussian fits and residual plots shown. PAN calculates the residuals, r_i , using the following formula

$$r_i = \frac{y_i^{\text{fit}} - y_i^{\text{data}}}{\sigma_i}, \quad (1)$$

where σ_i are the uncertainties on y_i^{data} . The upper example represents an instance where two Gaussian components are needed to fit the profile – with the inclusion of a second Gaussian the fit χ^2 is dramatically reduced and the residuals fall within the ± 1 guidelines. The lower plots show an example of a profile which is best fit with a triple Gaussian model. The addition of a second narrow, bright component as well as the broad, faint component causes a significant reduction in the χ^2 and again the residuals fall within the ± 1 guidelines.

We also applied a number of physical tests to further improve the accuracy of the results. First, for a fit to be accepted, the measured FWHM had to be greater than the associated error on the FWHM result (a common symptom of a bad fit), and secondly the FWHM had to be smaller than 15 Å (to guard against fitting continuum or spurious features). We also applied some additional filtering in order to ensure the first Gaussian component always corresponds to our definition of the first component [i.e. if $\text{flux}(C1) < \text{flux}(C3)$ AND $\text{fwhm}(C1) < \text{fwhm}(C3)$ then swap C3 with C1]. This only applies when the line contains three components and is sufficiently well resolved to reliably fit them all.

The bright [O III] λ 5007 line also exhibits the general line profile shape described above (narrow bright component with underlying fainter broad component), but unfortunately due to an instrumental artefact present at low levels in the blue wing of the line, we have not been able to characterize the shape of the secondary components accurately. The flux, width and velocity maps of the main bright [O III] λ 5007 component (C1) look very similar to the equivalent H α maps, so we do not show them here. Measurements of the [O III] λ 4959 line also result in similar flux, FWHM and velocity distributions, but since it is a weaker line we cannot fit the low-intensity broad component with any confidence.

4.2 How well can we fit each component?

The χ^2 minimization algorithm used by PAN is very sensitive to the uncertainties associated with the input spectra. Because of this, we paid special attention to creating accurate Poissonian error arrays

Table 4. Wavelength limits used in fitting each line.

Spectral line	Wavelength (Å)
H β	4840–4880
[O III] λ 5007	4940–5020
[O I] λ 6300	6250–6308
[N II] λ 6583	6570–6595
H α	6550–6575
[S II] λ 6717	6700–6724
[S II] λ 6731	6720–6750

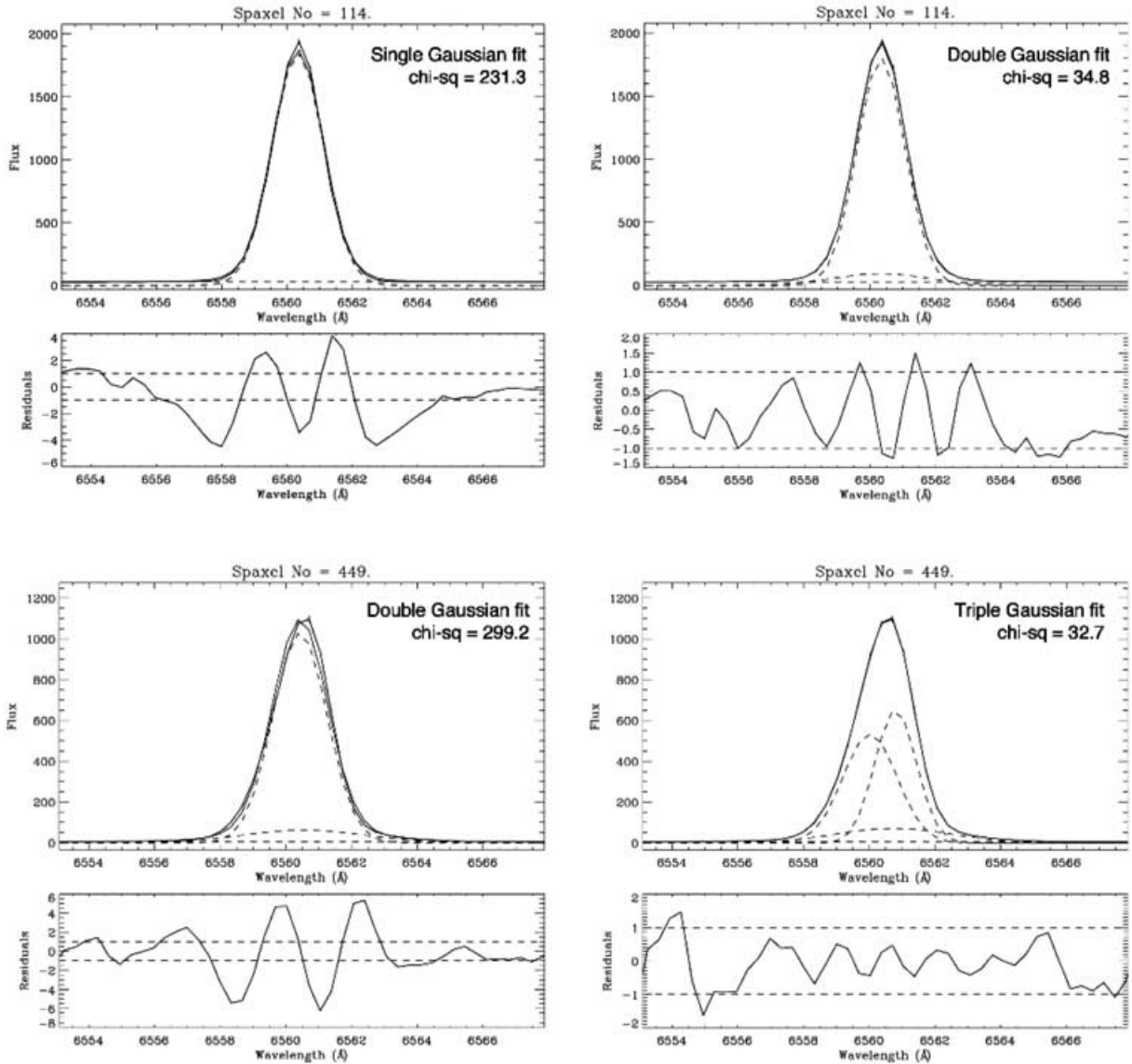


Figure 5. Examples of $H\alpha$ line fits made by PAN comparing a single and double Gaussian fit for spaxel 114 and a double and triple fit for spaxel 449 (y-axis in arbitrary flux units, but note the difference in scale). The black solid line is the observed data and the dashed lines represent the individual Gaussian components. Below each graph is a plot of the residuals (in units of σ) with dashed guidelines plotted at ± 1 (see text for an explanation of how the residuals are calculated). By comparing the ratios of the χ^2 values, the significance of a higher number of fit components can be tested.

from the raw uncalibrated spectra, which we then associated with the fully reduced spectra for the purposes of fitting (see Section 4.1). We made a number of tests comparing the results of Gaussian fits to high-S/N arc lines made with PAN with those output by other line fitting routines (such as ELF within the STARLINK DIPSO program). We found that despite differences in the minimization techniques employed, results and uncertainties quoted were very similar, and that PAN produced more consistent values across the whole wavelength range. We are therefore confident with the quality of results derived by PAN.

For a consistency check on the variability of the instrumental profile, we performed Gaussian fits to the unresolved $[O\text{I}]\lambda 5577$ telluric emission line on pre-sky-subtracted spectra. The spatial distribution of the fit components clearly show no systematic variability across the IFU field indicating that the line profile shape is very stable. We also find that the telluric line is well fitted by a single Gaussian,

and shows no evidence for broad wings. The $[O\text{I}]$ line fluxes have a standard deviation, $\text{s.d.} = 1.5 \times 10^{19} \text{ erg s}^{-1} \text{ cm}^{-2} \text{ arcsec}^{-2}$, the FWHM $\text{s.d.} = 4.5 \text{ km s}^{-1}$ and radial velocity $\text{s.d.} = 1.9 \text{ km s}^{-1}$.

We now turn to the uncertainty estimates on each line component's Gaussian properties (line centre, flux and width). Unfortunately, the errors that PAN quotes on its fit results are derived simply from the formal errors on the χ^2 minimization, and we have found these to be an underestimate of the true uncertainties. More realistic errors have been estimated through visual inspection of the fit quality taking into account noise in the continuum (i.e. S/N of line) and the number of fitted components. For the $H\alpha$ line flux, the percentage error varies between 0.5 and 10 per cent for C1 (for high–low S/N lines), 8–15 per cent for C2 and 10–80 per cent for C3. The addition of multiple Gaussian components always increases uncertainties; we estimate that where we can fit a third component, the errors in the flux of C1 and C2 increase by 5–10 per cent. For estimation

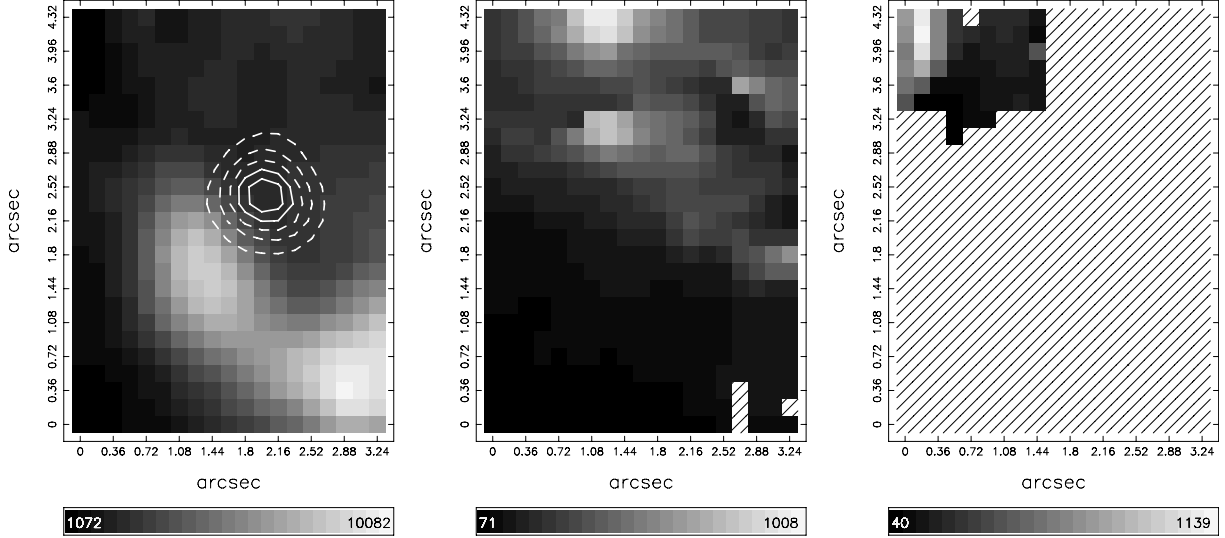


Figure 6. Left-hand panel: flux map in H α component 1 (C1; bright, narrow); central panel: flux map in H α component 2 (C2; faint, broad); right-hand panel: flux map in H α component 3 (C3; narrow, second peak). Non-detections are represented as hatched spaxels, the x and y scales are in arcseconds offset from the lower left-hand spaxel, and a scale bar is given for each plot in units of $10^{-15} \text{ erg s}^{-1} \text{ cm}^{-2} \text{ arcsec}^{-1}$. North is up and east is towards the left-hand side. The higher levels in the continuum image are plotted as contours on the left-hand plot, identifying the position of cluster 10.

of the FWHM and radial velocity errors, we have compared fits to the two lines of the [O III] $\lambda\lambda 4959, 5007$ doublet where possible. We find the FWHM errors vary between 0.25 and 2 km s^{-1} for high–low S/N C1 lines, respectively, 4 – 15 km s^{-1} for C2 and 15 – 20 km s^{-1} for C3. For the radial velocity, the error in C1 varies between 0.1 and 3 , 2 and 5 km s^{-1} for C2 and 10 and 30 km s^{-1} for C3. We estimate that the addition of a third component (where required) increases the errors in the C1 and C2 FWHM by $\sim 5 \text{ km s}^{-1}$ and the central velocity by $\sim 3 \text{ km s}^{-1}$.

4.3 Visualization of the data products

A major hurdle in the analysis of IFS is the visualization of the data products. To this end, we have developed a PERL/PGPLOT based plotting and analysis package nicknamed ‘DAISY’ that has enabled us to map out the results that we have obtained from our data set. We have already shown one such visualization in Fig. 2. The program allows the user to correct for DAR (currently not implemented), correct the measured FWHMs for the intrinsic instrumental profile (via simple FWHM² subtraction), deredden the data using the intrinsic H α /H β ratio method, convert wavelengths and FWHM into velocities, create a number of ratio combinations and then to visualize the results. There are options to allow the user to select the colour range (linear or log) for each plot, and to overplot using contours. Once fully developed, our aim is to release this package to the community.³

5 EMISSION-LINE MAPS

Figs 6–8 show maps of the fitted Gaussian properties (flux, FWHM and radial velocity) for each H α line component (we show maps for measurements of the H α line only for the reasons given above in Section 4.1) over the whole field. The grids represent that of our interpolated, cubed data, not the original GMOS configuration, and

the position of the cluster is overlaid with flux contours on selected maps to aid description and interpretation. As described in Section 4.1, in general we find a bright, narrow component overlaid on fainter, broad emission. This H α broad component reaches a corrected FWHM of $\sim 300 \text{ km s}^{-1}$ in places. In a number of spaxels we have been able to fit a third component (C3), which has approximately the same width as C1 implying that it may be associated with expanding shell- or bubble-like structures in the ionized gas.

5.1 H α maps

5.1.1 Component 1 (C1)

From Fig. 6, it is immediately obvious that C1 and C2 do not originate in the same place, i.e. the flux maps show strikingly different spatial distributions. The two main knots of emission in C1, located near the middle and south-west of the field (south of the cluster), correspond to the pattern of diffuse emission seen in both the WFPC2 F656N (Fig. 1) and ACS F555W (Fig. 2) images. These knots lie just to the south of cluster 10 and mark the easternmost extent of the large ionized complex seen in Fig. 1 (H II region 2; Waller 1991). The width of C1 shown in Fig. 7 (left-hand panel) ranges from an FWHM of ~ 30 – 40 km s^{-1} (corrected for instrumental broadening) towards the eastern side of the field, to $\sim 60 \text{ km s}^{-1}$ seen in a region arcing round to the west of cluster 10. This is coincident with the strip in between two linear filaments seen to the north-west of cluster 10 in Fig. 1, and may be indicative of an influence from the two SNRs located to the north of the FOV. A gradient in FWHM from ~ 35 to 45 km s^{-1} is centred on the position of the bright H α knot in the centre of the field, with broader widths seen on the side facing cluster 10, but the linewidth stays constant to within $\sim 5 \text{ km s}^{-1}$ over the extent of the cluster. As shown by the C1 radial velocity map (Fig. 8, left-hand panel), we see a region of material moving at $\sim -10 \text{ km s}^{-1}$ in the centre (just to the south of the cluster) surrounded by a ring of material with a velocity decreasing down to the systemic value. There is also an area of gas just to the north moving with a radial speed of $\sim +7 \text{ km s}^{-1}$. It is worth noting that

³ Interested users should contact Katrina Exter.

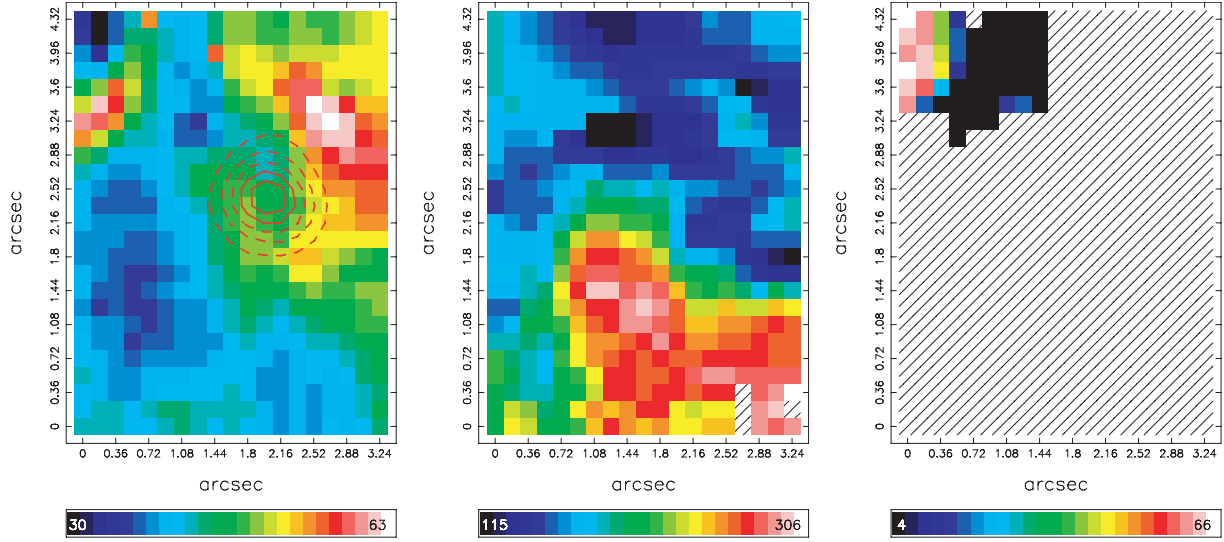


Figure 7. Left-hand panel: FWHM map in H α C1; central panel: FWHM map in H α C2; right-hand panel: FWHM map in H α C3. A scale bar is given for each plot in km s^{-1} units corrected for instrumental broadening. North is up and east is towards the left-hand side, and the position of cluster 10 is identified on the left-hand plot.

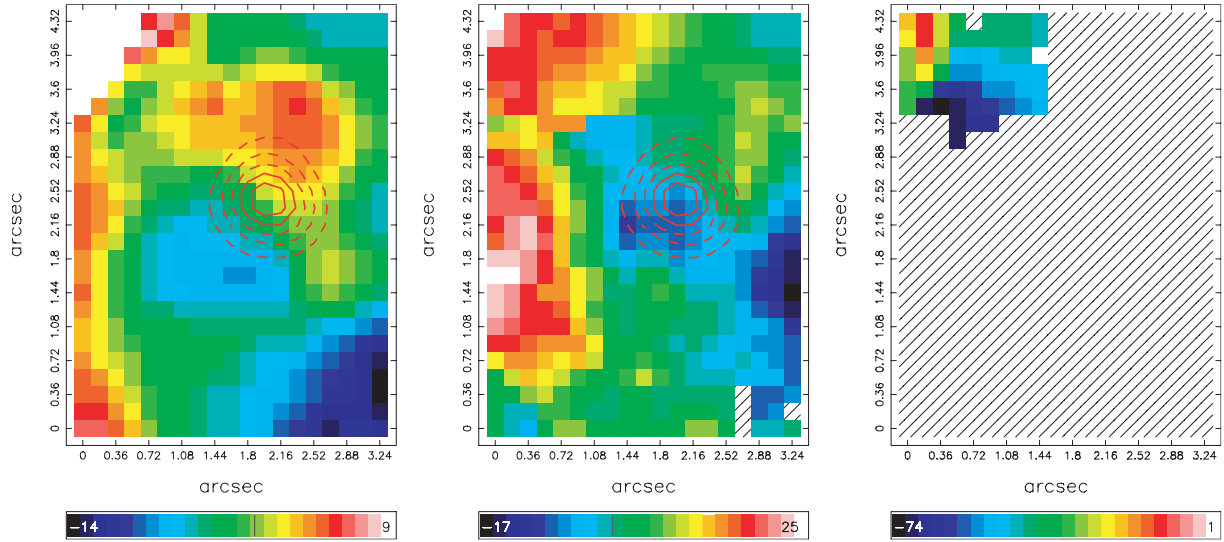


Figure 8. Left-hand panel: radial velocity map in H α C1; central panel: radial velocity map in H α C2; right-hand panel: radial velocity map in H α C3. A scale bar is given for each plot in units of km s^{-1} (heliocentric) relative to the systemic velocity of the region (-80 km s^{-1}), where zero is marked with a line. The position of cluster 10 is identified on the left-hand and central plots for comparison.

these regions of negative and positive velocities are located either side of the position of the cluster at approximately equal distances. The fastest radially approaching C1 gas is seen in the south-west, moving at $10\text{--}15 \text{ km s}^{-1}$ (coincident with the small dense knot seen in the *HST* H α image), and the fastest receding gas is found along the eastern edge, increasing to $\sim 15\text{--}20 \text{ km s}^{-1}$ (off the colour scale for this plot) in the far north-east. It should be borne in mind that the total C1 radial velocity range observed across the whole field is only $\sim 35 \text{ km s}^{-1}$.

5.1.2 Component 2 (C2)

The two small bright knots seen in C2 (Fig. 6, centre) towards the north of the field (north-east of cluster 10) do not correspond to

anything seen in the *HST* images. This is understandable since the most intense emission in C1 is an order of magnitude brighter than that in C2. The distribution of C2 FWHMs (Fig. 7, centre) is almost precisely anticorrelated with the line flux (Fig. 6, centre), where the brightest features exhibit the narrowest linewidth ($115\text{--}125 \text{ km s}^{-1}$). The left-hand panel of Fig. 9 better illustrates this by showing contours of C2 flux overlaid on the C2 FWHM map. The broadest C2 lines ($\sim 300 \text{ km s}^{-1}$) are seen in the south centre extending to the south-west of the field, corresponding well with the position of the brightest knots seen in C1 (Fig. 6, left-hand panel) and the WFPC2 image. This again is illustrated clearly in Fig. 9 (right-hand panel), where contours of C1 flux are overlaid on the C2 FWHM map. The C2 radial velocity field (Fig. 8, centre) covers the same overall range as the C1 gas; material approaching us at velocities of $\sim 15 \text{ km s}^{-1}$

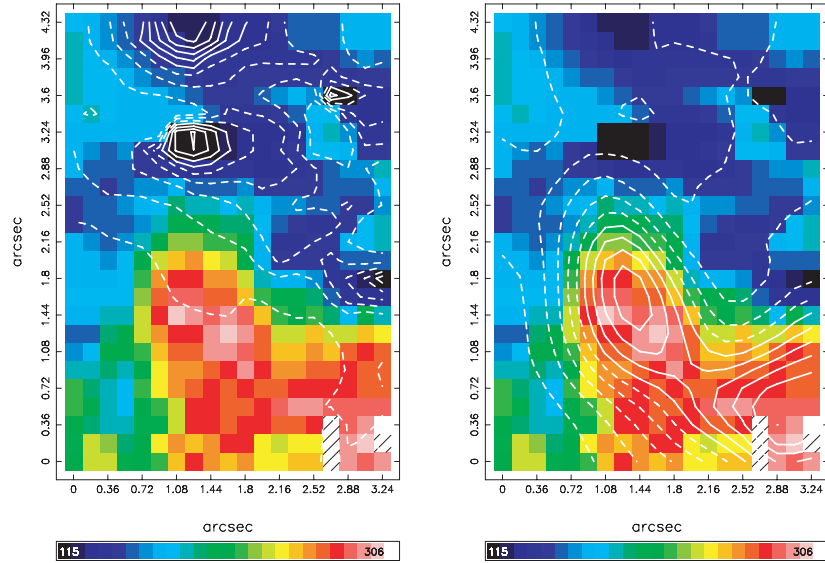


Figure 9. Left-hand panel: contours of C2 flux overlaid on the C2 FWHM map. Solid contours represent levels above the mean of the range, and dashed below the mean. Notice the precise correlation between areas of high flux and low FWHM in the north. Right-hand panel: contours of C1 flux overlaid on the C2 FWHM map. Here the correlation between the bright H α knots seen in C1 and the broadest C2 lines can be seen clearly.

(shown in blue) is located near the northern face of the bright C1 knot in the centre of the field, in between the negative and positive velocity regions in C1 and almost coincident with cluster 10. This area of approaching gas also extends towards the west, reaching a maximum approaching velocity of 20 km s^{-1} . The fastest receding C2 velocities (red) are found along the eastern edge of the field at $\sim 20\text{--}25 \text{ km s}^{-1}$ relative to the average. The spatial distribution of this region of redshifted gas mimics that of the redshifted C1 gas, but extends further to the west. Note the distribution of C2 radial velocities does not correlate with either of the C1 or C2 flux maps; however, we do tentatively point out a possible radial velocity difference of $\sim 25 \text{ km s}^{-1}$ between the two bright C2 knots seen in the flux map (Fig. 6, centre), and a spatial coincidence with the position of VLA-16 (a possible extended low surface brightness SNR).

5.1.3 Component 3 (C3)

A third component to the H α line profile fit was required in a small region located in the north-east of the field. The flux map (Fig. 6, right-hand panel) shows it is brightest in the far north-eastern corner and has an FWHM range (Fig. 7, right-hand panel) similar to C1. The radial velocity map (Fig. 8, right-hand panel) indicates that the C3 gas has a larger velocity towards our line of sight than any of the C1 or C2 gas (up to $\sim 70 \text{ km s}^{-1}$), but the associated uncertainties are large (see Section 4.2). Since our only detection of this third component is very near the edge of the field, it is difficult to estimate its extent or role from just these maps. Perhaps more interesting is the non-detection of a third component in locations where signatures of expanding structures might be expected from inspection of Fig. 1. We discuss the significance of this component in context with the whole central region and wind-blown cavity in Paper II.

5.2 Flux ratio maps

5.2.1 Electron density

Fig. 10 shows a plot of the spatial variation of electron density, n_e , as derived from the ratio between single Gaussian fits to the [S II] $\lambda\lambda$

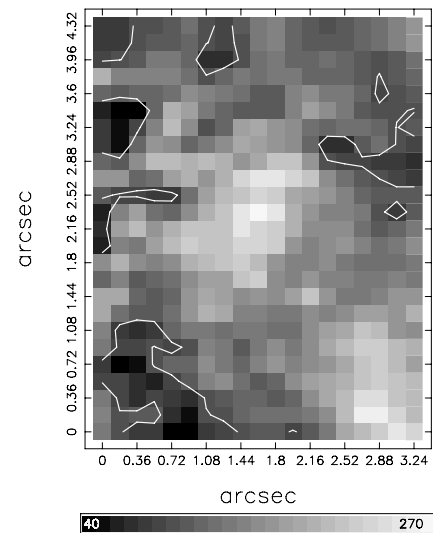


Figure 10. Map of the electron density, n_e , calculated from the ratio of single Gaussian fits to the [S II] $\lambda\lambda$ 6716, 6731 lines. The scale is in units of cm^{-3} . A single contour level marks the 100 cm^{-3} low-density limit.

6713, 6731 lines, assuming an electron temperature, T_e , of 10^4 K (the S/N of these lines is not high enough to fit multiple line components). There are two distinct regions of higher density seen in the map: in the south-west of the field, n_e reaches $\sim 250 \text{ cm}^{-3}$ and is spatially coincident with the south-western bright knot seen in H α C1 (Fig. 6, left-hand panel), and the small distinct knot seen in the *HST* F656N image. A second high-density region is coincident with the north-eastern part of the central bright H α C1 knot and the position of cluster 10, and peaks at $\sim 270 \text{ cm}^{-3}$. We derived the electron density of the H II region surrounding cluster 10 in Section 3, and found $n_e = 175^{+18}_{-20} \text{ cm}^{-3}$. Our peak value of 270 cm^{-3} is entirely consistent with this value since the spectrum for cluster 10 was created by summing 29 spaxels centred on this central density peak, and hence includes some dilution from the surrounding lower density gas. These values

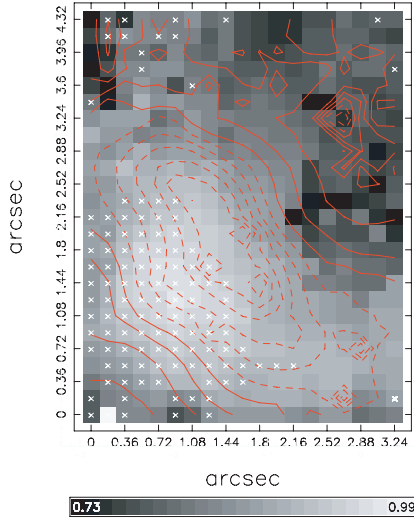


Figure 11. Flux ratio of $\log([O\text{ III}]\lambda 5007/H\beta)$ C1 (grey-scale; scale bar shown) with contours of the ratio $\log([S\text{ II}](\lambda 6717+\lambda 6731)/H\alpha)$ C1 (12 linearly spaced levels from -1.7 to -0.9). Spaxels marked with a cross indicate non-photoionized emission according to the maximum starburst line of Kewley et al. (2001).

are also consistent with Heckman et al. (1995), who find densities of up to $200 \pm 100\text{ cm}^{-3}$ in the central 15 arcsec of NGC 1569. Only a small proportion of the gas is at or below the low-density limit ($\sim 100\text{ cm}^{-3}$; Osterbrock 1989, shown by the single contour level on the map).

5.2.2 Nebular diagnostics

Our wavelength range gives us access to a number of important optical diagnostic lines that can be used to constrain the properties of the emitting gas. The flux ratio of $[O\text{ III}]/H\beta$ is a good reddening-free indicator of the mean level of ionization (radiation field strength) and temperature of the gas, whereas $[S\text{ II}]/H\alpha$ or $[N\text{ II}]/H\alpha$ are indicators of the number of ionizations per unit volume (ionization parameter; Veilleux & Osterbrock 1987; Dopita et al. 2000). A grey-scale representation of the observed C1 flux ratio of $[O\text{ III}]\lambda 5007/H\beta$ overlaid with contours of the $[S\text{ II}](\lambda 6717+\lambda 6731)/H\alpha$ C1 flux ratio is shown in Fig. 11. The ratio of $\log([S\text{ II}]/H\alpha)$ is lowest (-1.7 ; shown by dashed contours) where the flux in $H\alpha$ C1 is highest (see Fig. 6, left-hand panel), i.e. where the central bright knot is located. The peak of the $[O\text{ III}]/H\beta$ ratio is also near to the central bright $H\alpha$ knot, but offset by ~ 4.5 arcsec to the south-east. Numerically, the field average ratio of $\log([S\text{ II}]/H\alpha) = -1.29 \pm 0.17$, $\log([N\text{ II}]/H\alpha) = -1.62 \pm 0.16$ and $\log([O\text{ III}]/H\beta) = 0.87 \pm 0.05$ (1σ errors), showing that the variations in the ratios are really only small. Plotting these values on the standard diagnostic diagrams of the type first proposed by Veilleux & Osterbrock (1987) shows that all the points lie tightly clustered in the upper left-hand side of the starburst- $H\text{ II}$ region distribution. Comparing these values with the Mappings-III photoionization models of Dopita et al. (2000) for an instantaneous burst of star formation whose SED is given by SB99 (Leitherer et al. 1999), the gas is of low metallicity ($\sim 0.2 Z_{\odot}$) and has a high ionization parameter ($q \simeq 10^8$), as expected. Buckalew & Kobulnicky (2006) use *HST*/WFPC2 narrow-band imaging to calculate the ratios of $[O\text{ III}]/H\beta$ and $[S\text{ II}]/H\alpha$, and use the theoretical ‘maximum starburst line’ derived by Kewley et al. (2001) to set a threshold to de-

termine the difference between photoionized and non-photoionized emission. Using this criterion on our dereddened line ratios, we find a total of 118 spaxels containing possible non-photoionized emission, the location of which are plotted on Fig. 11 with white crosses. We note here that the threshold derived by Kewley et al. is a maximum in the sense that no pure starburst, regardless of metallicity (in the range $0.1\text{--}3 Z_{\odot}$) or ionization parameter, could produce emission above this line. A lower metallicity, such as found in NGC 1569, decreases the level of this theoretical limit, but since the model predictions are quite uncertain, understanding how many more points may have a non-photoionized contribution to their emission is non-trivial. For this reason, we have employed the more robust ‘maximum’ threshold.

The distribution shown in the map corresponds well to the maps of Buckalew & Kobulnicky (2006), with the majority of points lying in the south-east of the field. Since SSC A is located only 7 arcsec away in this direction, Buckalew & Kobulnicky (2006) associate these points with an ‘arc’ of non-photoionized gas resulting from a possible wind–wind interaction between the two clusters.

5.2.3 Reddening map

Dereddening with our visualization and analysis package uses the Galactic law of Howarth (1983, $R_V = 3.1$) and the intrinsic $H\text{ I}$ ratio of $H\alpha/H\beta = 2.85$ (Storey & Hummer 1995, for gas at $T_e = 10^4\text{ K}$ and $n_e = 100\text{ cm}^{-3}$). A reddening map, computed using only C1 of $H\alpha$ and $H\beta$, is shown in Fig. 12. The mean and standard deviation for $c(H\beta)$ for C1 over the FOV is 1.01 ± 0.16 (compared to 1.15 when summing the flux in all components for the $H\text{ I}$ lines). In this, we are assuming most of the reddening comes from a Galactic foreground screen (a valid assumption; Israel 1988; Origlia et al. 2001, Section 3). The reddening distribution is consistent with the location of the central and south-western bright knots seen in C1, where these knots exhibit the highest extinction [$c(H\beta) = 1.3 \equiv E(B - V) = 0.8$]. Interestingly, high values are also found in the north-west of the field, not correlating with any feature on any of the other maps. The lowest reddening [$c(H\beta) = 0.75 \equiv E(B - V) = 0.5$; equivalent to the Galactic foreground level; Relaño et al. 2006]

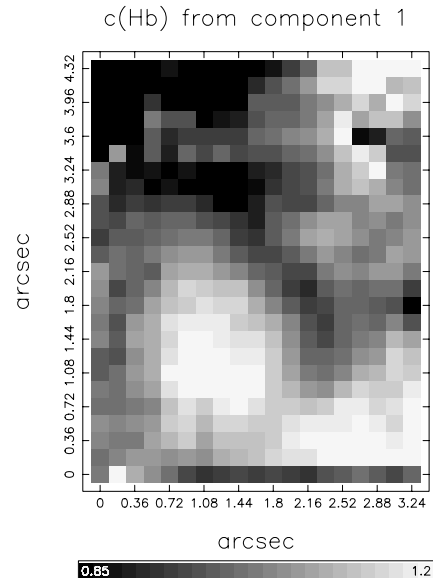


Figure 12. A $c(H\beta)$ map calculated from the C1 flux ratio of $H\beta/H\alpha$.

is found in the north-east of the field, coincident with the location of the group of spaxels containing C3.

6 INTERPRETATIONS AND DISCUSSION

At the distance of NGC 1569, the GMOS IFU FOV covers $\sim 50 \times 35$ pc with an 8-pc resolution, and is therefore ideal for studying the detailed relationship between young star clusters and their environment. To this end, we have observed a region near the centre of the galaxy covering one such young, bright star cluster and the surrounding ionized gas. Taking advantage of the spatially resolved nature of IFU observations, we extracted a spectrum of the cluster to derive its fundamental properties, and created well-defined, high-S/N maps of the Gaussian properties of each observed H α line component across the FOV. In the following sections we discuss our findings relating to the cluster itself and to the surrounding ionized gas. We also explore possible theories that might give rise to the observed broad emission profiles and discuss their consequences.

6.1 Cluster 10

As clearly seen in the high-resolution *HST*/ACS images (Fig. 2), cluster 10 is composed of two individual clusters which we denote 10A and 10B. We measure their projected separation to be ~ 3.7 pc and their sizes to be $R_{\text{eff,A}} = 0.88$ and $R_{\text{eff,B}} = 0.60$ pc, and a combined photometric mass of $7 \pm 5 \times 10^3 M_{\odot}$. By comparing the relative photometry of each cluster we find them to have very similar ages: 10B is the youngest (< 5 Myr) and 10A a little older (5–7 Myr). The combined spectrum of the two clusters extracted from our IFU data shows that one (or both) of these clusters has a significant population of WR stars.

The unusually compact nature of these two clusters is reminiscent of R136 in the LMC. This equally young cluster has an $R_{\text{eff}} \approx 1.7$ pc and mass of a few $\times 10^4 M_{\odot}$ (Hunter et al. 1995; Bosch et al. 2001). R136 contains a large number of massive stars that power and maintain the ~ 100 pc diameter giant H II region 30 Dor.

Our age estimates of the two clusters show that their formation was approximately coeval with SSC A, and that vigorous star formation has certainly occurred recently in NGC 1569. Cluster 10 is located within the bright H II region no. 2 (Waller 1991) which is found to emit a powerful thermal radio signature (Greve et al. 2002) and bright mid-IR forbidden line and continuum emission (Tokura et al. 2006). These observations imply that this whole area is a large embedded star formation complex being fuelled by the neighbouring molecular CO cloud (Taylor et al. 1999).

We do not see evidence for a compact individual H II region surrounding the cluster in the H α flux maps or the extinction map. This is probably because the winds and SN events have blown away the surrounding gas. The electron density map, however, does show an enhancement at the location of cluster 10, indicating that perhaps there is some associated gas remaining. Our IFU FOV contains a great deal of ionized material that is both influenced by cluster 10 and by the relatively distant, but more massive, SSCs A and B. It is not clear if the source of ionization for H II region 2 is solely cluster 10 or whether other starburst regions contribute.

6.2 Ionized gas

6.2.1 The turbulent ISM and the narrow component (C1)

The integrated H I velocity dispersion for the disc of NGC 1569 is $\sigma \approx 15 \text{ km s}^{-1}$ (FWHM $\approx 35 \text{ km s}^{-1}$) indicating that the neutral

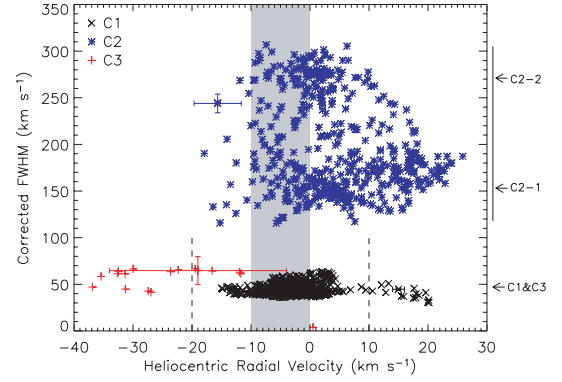


Figure 13. H α linewidth (FWHM, corrected for instrumental broadening but not thermal broadening of $\sim 20 \text{ km s}^{-1}$) versus centroid velocity (heliocentric, relative to the systemic velocity of the region, $v_{\text{sys}} = -80 \text{ km s}^{-1}$). A representative error bar has been plotted for each of the three components on one selected data point. The shaded region represents the velocity (including the error) of cluster 10 (see Section 3). Next to the right-hand axis are labels marking the three regimes in FWHM discussed in the text. C1 (C3) points lying to the right-hand side (left-hand side) of the vertical dashed lines form the high-velocity tails referred to in the text.

ISM is very disturbed (Mühle et al. 2005), presumably due to the combined effects of stellar winds and SNe. This value is consistent with the broad linewidths also found in H I clouds associated with nearby giant H II regions (Viallefond, Allen & Goss 1981). We would thus expect the H II gas in NGC 1569 to have similar or higher velocity dispersions to the H I.

In Fig. 13 we plot the heliocentric radial velocity against linewidth for all identified line components across the FOV, whilst in Fig. 14 we plot the line flux against linewidth. This latter plot was used successfully as a diagnostic tool by Muñoz-Tuñón et al. (1996, see also Martínez-Delgado et al. 2007) to examine the physical origin of the broadening mechanisms in giant H II regions. Plotting the line

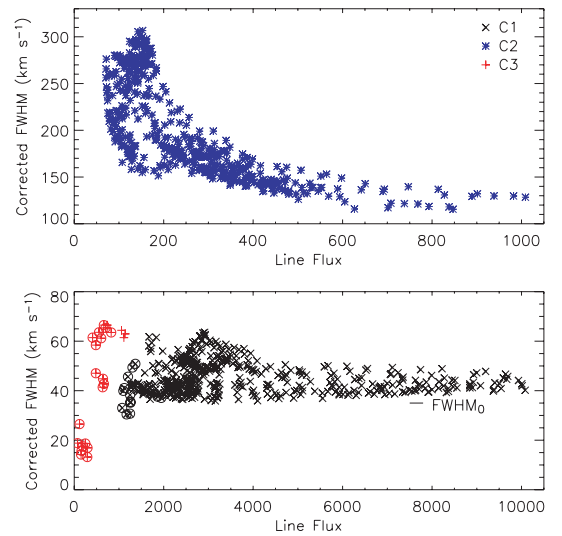


Figure 14. H α linewidth (FWHM, corrected for instrumental but not thermal broadening) versus flux (arbitrary scale). The selected axis ranges show C1 and C3 in the lower panel, and C2 in the upper panel (note in particular the factor of 10 difference in flux range). The distinct lower limit to the FWHM of C1, $\text{FWHM}_0 \approx 35 \text{ km s}^{-1}$, is marked. Encircled points are those belonging to the high-velocity tails referred to in the text and defined by the vertical dashed lines in Fig. 13.

characteristics in this way highlights a number of trends within and between the components.

Fig. 13 shows that components C1 and C3 ($\text{FWHM} = 35\text{--}65 \text{ km s}^{-1}$) are easily distinguished from component C2 ($\text{FWHM} = 120\text{--}300 \text{ km s}^{-1}$). Furthermore, in the bottom panel of Fig. 14, a distinct $\sim 35 \text{ km s}^{-1}$ lower limit to the C1 FWHM (which we henceforth refer to as FWHM_0) can be seen. After correction for thermal broadening ($\sim 20 \text{ km s}^{-1}$ at $T \sim 10^4 \text{ K}$), this becomes 29 km s^{-1} (or $\sigma \approx 12 \text{ km s}^{-1}$), meaning the C1 line velocity widths correspond to mildly supersonic speeds (for $T_{\text{gas}} = 10^4 \text{ K}$, the sound speed is $\sim 10 \text{ km s}^{-1}$). We note that the C1 linewidth does not correlate strongly with line flux, unlike the broad component (C2) which we discuss below.

The red velocity tail of C1, seen clearly on Fig. 13 as points lying to the right-hand side of the vertical dashed line at velocity $= +10 \text{ km s}^{-1}$, corresponds spatially to the extreme north-east of the field where we also see a blueshifted component (C3; see e.g. Fig. 5, lower panels). These C3 points lie to the left-hand side of dashed line at velocity $= -20 \text{ km s}^{-1}$. The velocities of these double-peaked emission lines are distributed evenly to the red and blue of the cluster radial velocity (shown as a grey strip), providing the only signature of classical shell expansion in the field. Furthermore, the two components have similar flux levels as illustrated in Fig. 14 (see also Fig. 5, lower right-hand panel), where the corresponding high-velocity C1 and C3 points are plotted with encircled symbols.

Broad linewidths have been observed in many young star-forming regions e.g. 30 Dor or NGC 604 (Chu & Kennicutt 1994; Yang et al. 1996). A search through the literature uncovers a number of alternative theories that could account for the observed linewidths of C1, including electron scattering, multiple unresolved expanding shells integrated along the line of sight, and gravitational broadening through virial motions.

Electron scattering can be immediately ruled out, as unphysical electron densities are required to produce the observed widths (see Roy et al. 1992). Multiple unresolved expanding shells integrated along the line of sight was an explanation proposed by Chu & Kennicutt (1994) to explain their observed broad linewidths in the giant H II region 30 Dor. A follow-up study of the same region by Melnick et al. (1999), but at very high spatial and spectral resolution (0.6 arcsec seeing and $0.067 \text{ \AA pix}^{-1}$), allowed shells to be resolved down to their resolution limit of 0.13 pc . In their observations, the broad linewidths found by Chu & Kennicutt 1994 were resolved into a myriad discrete narrow lines representing individual shell components, thus validating the conclusions of Chu & Kennicutt (1994) when observations are made at insufficient spatial/spectral resolution.

However, an analytical model for this unresolved shells effect, first developed by Dyson (1979) and analysed in detail by Tenorio-Tagle, Muñoz-Tuñón & Cid-Fernandes (1996), predicts that if the age distribution of the stars powering the expanding shells is greater than the time-scale for gravitational collapse of the parent cloud, the resulting line profiles are always flat-topped. This is something we do not see. Since the spatial and spectral resolution of our observations is $\sim 9 \text{ pc}$ and $0.34 \text{ \AA pix}^{-1}$, it is conceivable that a contribution to the narrow linewidth is due to unresolved expanding shells. However, since the point at which coherent shells break up is when their expansion velocity equals the ambient ISM turbulent velocity (FWHM_0), unresolved expanding shells cannot contribute significantly to the observed widths of C1.

Furthermore, Tenorio-Tagle et al. (1996) find that to have a collection of unresolved shells capable of producing a supersonic linewidth over a large range of densities implies a great many low-

energy winds with properties similar to those typical for low-mass stars. If multiple shells are responsible for the observed broadening in our case, then the level of broadening would be expected to scale to a certain degree with gas column density (a large volume of gas could contain shells with a larger range of velocities), but this is not observed. The broadest C1 lines are seen in the north-west of the field, away from the bright knots in the field centre.

Gravitational broadening has been suggested by a number of authors as an explanation for the observed linewidths in giant H II regions (Melnick 1977; Terlevich & Melnick 1981; Tenorio-Tagle, Muñoz-Tuñón & Cox 1993), and predicts that the line profile should be approximated by $\sigma_{\text{virial}} = \sqrt{GM/R}$. This explanation has been successfully used to explain and calibrate the $R \propto \sigma$ and $L \propto \sigma$ relations found for giant H II regions (Terlevich & Melnick 1981; Melnick, Terlevich & Moles 1988), and explain the supersonic widths found in NGC 604 (Muñoz-Tuñón et al. 1996; Yang et al. 1996). Although NGC 1569 cannot be likened to a single giant H II region, we can make a crude estimate of the expected virial broadening by taking the mass to be the total H I mass of the galaxy $M_{\text{H I}} \sim 10^8 M_{\odot}$ (Mühle et al. 2005) and an isophotal radius of $\sim 4 \text{ kpc}$ (de Vaucouleurs et al. 1991; Mühle et al. 2005). This results in a broadening of $\sigma_{\text{virial}} \approx 11 \text{ km s}^{-1}$, in surprising agreement with our measured FWHM_0 .

Thus, in conclusion we find that C1 represents the turbulent ISM, where its motions result from a convolution of both the underlying gravitationally induced virial motions inherent in the gas and the general stirring effects of the starburst. It is also possible that an additional minor contribution to its width may originate from unresolved shell components along the line of sight.

6.2.2 The broad component, C2

We now turn our attention to the intriguing broad component (C2). In the following discussion, we will attempt to understand what the conditions of the emitting gas are, and what mechanism(s) are acting to give it such a broad width. First, we can use Figs 13 and 14 to identify a number of trends to help constrain the physical properties of this component. Fig. 13 shows that the group of C2 points can be split into two further subgroups. The narrower group ($\text{FWHM} \approx 150 \text{ km s}^{-1}$; labelled C2-1 on the plot) is associated with the regions of higher C2 flux (compare the central panels of Fig. 6 with Fig. 7), whereas the close grouping of high-FWHM C2 measurements ($\approx 280 \text{ km s}^{-1}$; labelled C2-2) correspond (to a high degree of correlation) with the most intense C1 emission (i.e. the two bright knots; see Fig. 9, right-hand panel). Disregarding the red tail of the C1 velocity distribution discussed earlier, there is an average redward offset of only $\sim 10 \text{ km s}^{-1}$ between C1 and C2, implying that C2 does not originate from gas with large-scale bulk motions. Fig. 14 clearly demonstrates that the broadest C2 lines are also the faintest (a common result; Muñoz-Tuñón et al. 1996), where the average ratio of $\text{flux}(\text{C2})/\text{flux}(\text{C1})$ over the FOV is 0.07. We can now assert that any theory explaining the origin of C2 must describe both how it exists over the entire FOV, and why its width is at once so highly correlated with the position of the bright knots seen in the narrow component, and so anticorrelated with its own flux.

Mechanisms proposed in the literature that can account for linewidths of $>100 \text{ km s}^{-1}$ in H II regions are quite varied, particularly from studies of more distant systems. Moreover, there are few studies that compare in terms of both the spatial scale of the overall region (i.e. 30 Dor, e.g. is clearly much smaller than the

NGC 1569 starburst) and the spatial resolution of the observations. This makes it harder to evaluate which mechanisms may be at work in NGC 1569.

Unresolved expanding shells have again been cited as a possible cause of the broad component in a few studies, but it is difficult to envisage how smooth Gaussian profiles with widths of up to 300 km s^{-1} could be fully accounted for in this manner without showing some signs of velocity splitting at our level of spectral resolution. Heckman et al. (1995) observed $\text{H}\alpha$ emission from NGC 1569 using two perpendicularly oriented long slits intersecting at SSC A, and in positions where they were able to fit multiple Gaussians to the line profile, they found two distinct kinematic systems. Lines near to v_{sys} were found to have widths of $\text{FWHM} \approx 30\text{--}90 \text{ km s}^{-1}$, whereas broader lines with widths of up to 150 km s^{-1} were only identified at radial velocities of over 200 km s^{-1} relative to v_{sys} . Heckman et al. proposed that this second, high-velocity system is the origin of the broad widths ($30\text{--}50 \text{ \AA}$ at full-width zero-intensity) found in the summed $\text{H}\alpha$ line profile of the area surrounding SSC A, since when integrating a larger spatial area, the discrete kinematic systems became blended together.⁴ The level of broadening due to unresolved components is therefore dependent on *both* spatial and spectral resolution. This is illustrated well by the study of Melnick et al. (1999), described above. Although their high spatial- and spectral-resolution observations allowed them to resolve individual line components (shells) on scales down to 0.1 pc , they were still able to identify a clear, underlying, broad component persisting in all sight lines.

Can the effects of high-energy photons and fast-flowing winds from the nearby clusters explain the origin of C2? Over the years, much work has been done examining these effects using complex hydrodynamical models (Hartquist, Dyson & Williams 1992; Klein, McKee & Colella 1994; Suchkov et al. 1996; Marcolini et al. 2005; Pittard et al. 2005; Tenorio-Tagic et al. 2006). An exchange of energy and mass between the different hot and cold phases of the ISM can occur through four main processes: photoevaporation; conductively driven thermal evaporation; hydrodynamic ablation; and turbulent mixing (for a review see Pittard 2007). Photoevaporation takes place in the presence of a strong ionizing radiation field, and conductive evaporation occurs when energetic electrons from a hot, surrounding medium, deposit their energy in the cloud surface. When the hot, tenuous medium is fast flowing, as in the case of stellar or cluster winds, shearing between the high-velocity flow and the cloud surface can set up a turbulent mixing layer that can drive further evaporation. The impacting wind can also physically strip (ablate) material off the clump surface, and entrain it into the flow (Scalo 1987).

Begelman & Fabian (1990) described a model for a turbulent mixing layer that forms between the hot, intercloud gas and the surface layers of cool or warm clouds in near-pressure equilibrium. The UV radiation emitted from the mixing layer photoionizes the cold gas in the cloud surface giving rise to optical emission lines (in a similar way to a shock precursor) with characteristic velocities of a fraction of the hot-phase sound speed. Slavin, Shull & Begelman (1993) expanded on this idea by modelling the cloud interface in detail. Including the effects of non-equilibrium ionization and self-photoionization allowed them to predict a number of optical, IR and UV line ratios, which they found to be in good agreement with the

observed values at high latitudes in our Galaxy (for which this model was originally developed). Slavin et al. (1993) show a schematic of their model in their fig. 1: hot gas flows past a sheet of cold or warm gas inducing Kelvin–Helmholtz instabilities and the build-up of a turbulent mixing layer at the interface region. Thermal conduction between the layers results in a turbulent cascade down to the dissipative level, allowing the efficient exchange of energy between the media. Their model predicts strong optical [O III] and $\text{H}\alpha$ emission with non-Gaussian (broad-winged) line profiles caused by the high levels of turbulence. Strong far-UV emission from C IV and O VI is also predicted. These predictions are qualitatively in good agreement with what we observe, however, the Slavin et al. model predicts [O III]/ $\text{H}\beta$ and [S II]/ $\text{H}\alpha$ nebular line ratios firmly in the shocked regime, far away from our observed ratios. A decrease in the ‘maximum starburst’ line threshold (indicating gas with a shocked emission component) due to the low metallicity of NGC 1569 may account for part of this discrepancy.

It is interesting to note that observations of CO (e.g. Falgarone & Phillips 1990), CH^+ (Crane, Hegyi & Lambert 1991) and H_2 $2.1 \mu\text{m}$ (e.g. Geballe et al. 1986) in close-by Galactic molecular clouds have also revealed broad line profiles similar in shape to what we observe in our optical recombination and forbidden lines. To explain these observations, Hartquist et al. (1992) and Dyson et al. (1995) also developed turbulent boundary layer models, and found these broad molecular linewidths could again be reproduced through the presence of shear-induced turbulence, resulting from shocks in the cloud interface due to the viscous coupling between the fast wind and the clump gas. Melnick et al. (1999) were the first to suggest a connection with turbulent layers and erosion of dense gas clumps in an extragalactic environment when discussing the persistent underlying broad line component identified from their high-resolution observations of 30 Dor.

We therefore find the most likely explanation of the origin of C2 is emission from a turbulent mixing layer formed at the surface of dense clouds resulting from the viscous coupling between the cool clump material and the hot, fast, winds from the surrounding clusters. Material is also removed from this layer through thermal evaporation and/or mechanical ablation, resulting in the mass-loading of the flow. We know from X-ray studies that the hot, diffuse medium in NGC 1569 has a characteristic temperature around 0.7 keV ($\sim 10^7 \text{ K}$; Martin et al. 2002), implying that the sound speed in this hot phase is $\sim 500 \text{ km s}^{-1}$. The linewidths we measure are only 60 per cent this value, meaning that the turbulent motions are subsonic with respect to the hot gas. This may provide a further explanation for the lack of shock-excited line ratios in our data, since it is expected that photoionization in these central regions would overwhelm the signature of shock excitation anyway.

Although a shear-induced turbulent mixing layer can theoretically attain a quasi-steady state when the energy flux into the layer is equal to the cooling rate per unit area (Slavin et al. 1993), the additional destructive effects of evaporation and/or ablation mean that gas clumps will only have a limited lifetime. How long could we therefore expect the clouds to survive? Unfortunately our knowledge of cloud disintegration is not yet developed enough to answer this question in detail. Simple hydrodynamical simulations of ablation predict that clouds enveloped in a supersonic (relative to the cloud temperature) wind have survival time-scales typically less than 1 Myr (Klein et al. 1994; Marcolini et al. 2005). Clearly this cannot be the case since warm ionized gas is observed in superwinds out to heights of many kpc (e.g. Martin 1998; Shopbell & Bland-Hawthorn 1998; Devine & Bally 1999). Further detailed modelling work is required.

⁴ In our data, we associate C3 with part of the high-velocity system described by Heckman et al., and where detected, we resolve it at a sufficient level for it not to be confused with the broad C2.

Whether or not these mechanisms are all acting in our particular FOV, we conclude that the energetics are dominated by the interface layer at the surface of the gas clumps, and that the principle influence on the gas state is external to the clouds, rather than embedded within the cloud, as would be the case for isolated giant H II regions. In other words, the properties of the H α knots in our FOV are tied to the intrinsic state of the gas rather than the available energy supplies (the star clusters). This important difference may help to explain why the turbulent widths decrease away from the cloud surfaces. Cloud material remains intact and cool only for a limited length of time after it leaves the surface of the gas clump. Dense gas found near the surface of the cloud would be able to emit in H α at higher velocities as it becomes entrained into the high-velocity flow than less dense gas, resulting in a broader linewidth at the location of the cloud.

6.2.3 The motion of C2

The average width of C2 is much higher than the average radial velocity offset between C1 and C2 (obvious from comparing Figs 13 and 14), meaning that in our FOV, turbulent motions dominate over bulk flows. Tenorio-Tagle et al. (2006) develop 2D hydrodynamical models of the evolution of an H II region assuming that the medium surrounding the ionizing star cluster is composed of a large collection of clouds (i.e. a clumpy medium). Although their model is not specifically applicable to our case since the ionizing source is located within the cloud stratum, it illustrates a number of interesting results regarding the flow of material within the outer bounding shock front. In their simulations, the leading shock filters slowly through the gas clouds dissipating them one by one, leaving a highly turbulent, mass-loaded medium in its wake. The material interior to the leading shock moves in all directions resulting from the obstruction by the gas clumps, and possesses only a small net velocity in the outward direction. This is a very similar situation to what we observe, and shows that our FOV must be sampling gas well within the bounding shock (or sonic point) of the galactic wind, since as the flow becomes supersonic, turbulence is damped leaving only the bulk velocity component.

6.2.4 Final remarks

We find small-scale variations in the velocity fields of both C1 and C2 components, suggesting local energy inputs. However, these cannot (yet) be tied unambiguously to the effects of any single energy source (e.g. cluster 10). The distribution of non-photoionized emission covering the whole of the south-eastern portion of the FOV (see Fig. 11) would suggest that high-velocity gas is impacting from the south-east (i.e. the direction of SSC A), but without information on the 3D distribution of the gas and velocity field, we cannot be sure.

Since the constraints to our model of the origin of C2 are only qualitative, further observations and modelling are clearly required. We predict that if the energetics are dominated by the interface region where the turbulence is proposed to originate, observations of emission originating from deep within the cloud would not show this line broadening. This would also apply to regions shielded from the wind impact, where only the ambient ISM turbulence would be evident. Furthermore, the models of Marcolini et al. (2005) predict strong soft X-ray emission from the bow-shock (reverse shock) produced as the wind hits the cloud. Whether the X-rays are primarily emitted from wind material or evaporated cloud material depends

on the metallicity of the wind and the strength of the thermal conduction within the cloud. UV emission (or absorption) from C IV and O VI is also predicted to arise through collisional processes within the cloud material at the wind–cloud interface by both Slavin et al. and Marcolini et al. Currently, O VI-emitting gas is the highest temperature phase of an outflow that can be probed for which reliable velocities can also be measured (Heckman et al. 2001), making this transition a very important tool in the investigation of galactic winds.

In a companion paper (Paper II), we present the analysis of the other three IFU fields covering the central regions of NGC 1569. Following on from our analysis presented here, we first concentrate on the details of each field, then combine all the data in an attempt to constrain the general state of the ISM in the whole region.

7 SUMMARY

The unique capabilities of the GMOS IFU, coupled with *HST* imaging, have allowed us to map the detailed ionized gas properties of a 5×3.5 -arcsec² region near the nucleus of NGC 1569, and to relate the presence of a young star cluster located in the centre of the FOV to the surrounding gas. This field is part of a large, bright H II region complex (H II region 2; Waller 1991) that dominates the emission intensity, and exhibits evidence for recent, ongoing and embedded star and cluster formation, presumably fuelled by the large near-by repository of molecular gas (Taylor et al. 1999).

Summing the spectra from an aperture centred on the position of the cluster has allowed us to measure and derive a number of fundamental characteristics of this object. We draw the following conclusions.

- (i) Cluster 10 is composed of two subclusters, which we have denoted 10A and 10B, with sizes $R_{\text{eff,A}} = 0.88$ and $R_{\text{eff,B}} = 0.60$ pc and a projected separation of 3.7 pc. Because of their proximity, they cannot be resolved in our IFU data.
- (ii) Using model colour–colour diagrams, we were able to estimate their ages to be 5–7 Myr for 10A and ≤ 5 Myr for 10B, with reddenings consistent with the Galactic foreground level (confirmed by measurements of the H α /H β ratio from our IFU spectrum).
- (iii) We derive a photometric mass of $7 \pm 5 \times 10^3 M_{\odot}$ from the combined light of both subclusters. This result means that cluster 10 is not an SSC in the generally accepted definition.
- (iv) The presence of the red WR-bump (resulting from broad C IV emission) confirms the young age of at least one of the subclusters. From measuring the total luminosity of the feature, we estimate an equivalent population of 10 ± 5 WC4 stars in cluster 10. This is consistent with the narrow-band He II observations of Buckalew et al. (2000) who find emission associated with 10B equating to a luminosity equivalent of 3 WNL stars.

The spatially resolved nature of our observations has allowed us to make a detailed analysis of the distribution of gas within the FOV. The most important findings are as follows.

- (i) We find bright emission over the whole field well characterized by a Gaussian function with mildly supersonic linewidths (C1), and a distinct lower limit of $\text{FWHM}_0 \approx 35 \text{ km s}^{-1}$ (equating to $\sigma = 12 \text{ km s}^{-1}$ after correction for thermal broadening).
- (ii) We also measure a fainter line component (C2) with linewidths of between ~ 100 and 300 km s^{-1} , also found over the whole field.
- (iii) The width of the broad underlying emission is both highly correlated with the position of the bright narrow component

emission (i.e. bright C1 \propto broad C2), and anticorrelated with its own flux (i.e. bright C2 \propto narrow C2).

(iv) We conclude that C1 represents the turbulent ISM, where its motions result from a convolution of gravitational virial motions and the general stirring effects of the starburst (giving rise to the clear lower limit to the linewidth, FWHM₀). However, it is possible that an additional minor contribution to its width may originate from unresolved shell components along the line of sight explaining the local variations in C1 width across the FOV.

(v) We find the most convincing mechanism to explain the broad component is emission from a turbulent mixing layer on the surface of the cool gas clumps in the ISM of NGC 1569. This layer results from the coupling between the clump material and the hot, fast winds from the surrounding clusters, and gives rise, through thermal evaporation and/or ablation, to a tenuous, highly turbulent, diffuse gas that pervades the local environment that will eventually mass-load the outflow.

(vi) The distribution of non-photoionized (shocked) gas as determined from nebular diagnostic line ratios supports evidence that the dominant source of wind energy/material is from SSC A, consistent with morphological indicators such as swept-back cones around dense H α emitting knots that point towards this cluster. This does not mean, however, that the significant proportion of ionizing flux in this region does not come from the young cluster 10.

(vii) The average radial velocity offset between C1 and C2 is very small compared to the average linewidth of C2, indicating that in our FOV, turbulent motions dominate over bulk flows, and that we are sampling well within the ‘energy injection zone’ of the outflow.

Our results reflect the presence of a complex ISM with a wide range in physical conditions. Our suggestion that gas is being mixed from the relatively cool photoionized medium into the hot phase carries with it a number of astrophysical implications that could generally apply to galactic winds. Among these would be mass-loading of the hot ISM occurs close to or within the star-forming disc. This will enhance the hot ISM cooling rate and increase the density of material injected into the base of the thermal wind, thus influencing the properties of the wind. A full discussion of the ionized gas state in NGC 1569 will be presented in a companion paper (Paper II), where we put our findings for this IFU position in context with the whole central region using observations made with three other IFU pointings. In a forthcoming contribution (Paper III) we will examine the properties of the galactic outflow as a whole using deep H α imaging and IFU observations and attempt to create a unified physical picture of the outflow state.

ACKNOWLEDGMENTS

We thank the referee for their insightful comments and suggestions that have improved the paper. MSW thanks the Instituto de Astrofísica de Canarias (IAC) for their warm hospitality and financial support during the writing of this paper. MSW also wishes to thank Roberto Terlevich for interesting discussions on the origin of the line components. KME acknowledges the support from the Euro3D Research Training Network, grant no. HORN-CT2002-00305. The Gemini Observatory is operated by the Association of Universities for Research in Astronomy, Inc., under a cooperative agreement with the NSF on behalf of the Gemini partnership: the National Science Foundation (United States), the Particle Physics and Astronomy Research Council (United Kingdom), the National Research Council (Canada), CONICYT (Chile), the Australian Research Council (Australia), CNPq (Brazil) and CONICET (Argentina).

REFERENCES

- Ables H. D., 1971, *Publ. US Naval Obs.*, 20, 60
Allington-Smith J., Murray G., Content R., Dodsworth G., Davies R., Miller B. W., Jorgensen I., Hook I. et al., 2002, *PASP*, 114, 892
Anders P., de Grijs R., Fritze-v. Alvensleben U., Bissantz N., 2004, *MNRAS*, 347, 17
Arp H., Sandage A., 1985, *AJ*, 90, 1163
Arribas S., Mediavilla E., García-Lorenzo B., del Burgo C., Fuensalida J. J., 1999, *A&AS*, 136, 189
Begelman M. C., Fabian A. C., 1990, *MNRAS*, 244, 26p
Bosch G., Selman F., Melnick J., Terlevich R., 2001, *A&A*, 380, 137
Bruzual G., Charlot S., 2003, *MNRAS*, 344, 1000
Buckalew B. A., Kobulnicky H. A., 2006, *AJ*, 132, 1061
Buckalew B. A., Dufour R. J., Shopbell P. L., Walter D. K., 2000, *AJ*, 120, 2402
Chu Y.-H., Kennicutt R. C., 1994, *ApJ*, 425, 720
Crane P., Hegyi D. J., Lambert D. L., 1991, *ApJ*, 378, 181
Crowther P. A., Hadfield L. J., 2006, *A&A*, 449, 711
Crowther P. A., De Marco O., Barlow M. J., 1998, *MNRAS*, 296, 367
de Marchi G., Clampin M., Greggio L., Leitherer C., Nota A., Tosi M., 1997, *ApJ*, 479, L27
de Vaucouleurs G., de Vaucouleurs A., Corwin H. G., Jr, Buta R. J., Paturel G., Fouque P., 1991, *Third Reference Catalogue of Bright Galaxies*, Vols 1–3, XII. Springer-Verlag, Berlin, Heidelberg, New York
Devine D., Bally J., 1999, *ApJ*, 510, 197
Devost D., Roy J.-R., Drissen L., 1997, *ApJ*, 482, 765
Dimeo R., 2005, *PAN User Guide*, <ftp://ftp.ncnr.nist.gov/pub/staff/dimeo/pandoc.pdf>
Dopita M. A., Kewley L. J., Heisler C. A., Sutherland R. S., 2000, *ApJ*, 542, 224
Dyson J. E., 1979, *A&A*, 73, 132
Dyson J. E., Hartquist T. W., Malone M. T., Taylor S. D., 1995, in Lizano S., Torrelles J. M., eds, *Rev. Mex. Astron. Astrofis. Ser. Conf.*, Vol. 1, *Boundary Layers and Highly Supersonic Molecular Hydrogen Flows*. UNAM, Mexico, p. 119
Falgarone E., Phillips T. G., 1990, *ApJ*, 359, 344
Fruchter A. S., Hook R. N., 2002, *PASP*, 114, 144
Galliano F., Madden S. C., Jones A. P., Wilson C. D., Bernard J.-P., Le Peintre F., 2003, *A&A*, 407, 159
Geballe T. R., Persson S. E., McGregor P. J., Simon T., Lonsdale C. J., 1986, *ApJ*, 302, 693
González-Delgado R. M. et al., 1994, *ApJ*, 437, 239
González-Delgado R. M., Leitherer C., Heckman T., Cerviño M., 1997, *ApJ*, 483, 705
Greggio L., Tosi M., Clampin M., de Marchi G., Leitherer C., Nota A., Sirianni M., 1998, *ApJ*, 504, 725
Greve A., Tarchi A., Hüttemeister S., de Grijs R., van der Hulst J. M., Garrington S. T., Neininger N., 2002, *A&A*, 381, 825
Hartquist T. W., Dyson J. E., Williams D. A., 1992, *MNRAS*, 257, 419
Heckman T. M., Lehnert M. D., 2000, *ApJ*, 537, 690
Heckman T. M., Dahlem M., Lehnert M. D., Fabbiano G., Gilmore D., Waller W. H., 1995, *ApJ*, 448, 98
Heckman T. M., Sembach K. R., Meurer G. R., Strickland D. K., Martin C. L., Calzetti D., Leitherer C., 2001, *ApJ*, 554, 1021
Herbig G. H., 1995, *ARA&A*, 33, 19
Holtzman J. A., Burrows C. J., Casertano S., Hester J. J., Trauger J. T., Watson A. M., Worthey G., 1995, *PASP*, 107, 1065
Homeier N. L., Gallagher J. S., 1999, *ApJ*, 522, 199
Howarth I. D., 1983, *MNRAS*, 203, 301
Hummer D. G., Storey P. J., 1987, *MNRAS*, 224, 801
Hunter D. A., Hawley W. N., Gallagher J. S., 1993, *AJ*, 106, 1797
Hunter D. A., Shaya E. J., Holtzman J. A., Light R. M., O’Neil E. J., Jr, Lynds R., 1995, *ApJ*, 448, 179
Hunter D. A., O’Connell R. W., Gallagher J. S., Smecker-Hane T. A., 2000, *AJ*, 120, 2383
Israel F. P., 1988, *A&A*, 194, 24

- Izotov Y. I., Dyak A. B., Chaffee F. H., Foltz C. B., Kniazev A. Y., Lipovetsky V. A., 1996, *ApJ*, 458, 524
- Kewley L. J., Dopita M. A., Sutherland R. S., Heisler C. A., Trevena J., 2001, *ApJ*, 556, 121
- Klein R. I., McKee C. F., Colella P., 1994, *ApJ*, 420, 213
- Kobulnicky H. A., Skillman E. D., 1997, *ApJ*, 489, 636
- Krist J., 2004, *The TINYTIM User's Guide v. 6.3*
- Larsen S. S., 1999, *A&AS*, 139, 393
- Leitherer C. et al., 1999, *ApJS*, 123, 3
- Lisenfeld U., Israel F. P., Stil J. M., Sievers A., 2002, *A&A*, 382, 860
- Lisenfeld U., Wilding T. W., Pooley G. G., Alexander P., 2004, *MNRAS*, 349, 1335
- Maoz D., Ho L. C., Sternberg A., 2001, *ApJ*, 554, L139
- Marcolini A., Strickland D. K., D'Ercole A., Heckman T. M., Hoopes C. G., 2005, *MNRAS*, 362, 626
- Marlowe A. T., Heckman T. M., Wyse R. F. G., Schommer R., 1995, *ApJ*, 438, 563
- Martin C. L., 1998, *ApJ*, 506, 222
- Martin C. L., Kobulnicky H. A., Heckman T. M., 2002, *ApJ*, 574, 663
- Martinez-Delgado I., Tenorio-Tagle G., Munoz-Tunon C., Moiseev A. V., Cairos L. M., 2007, *AJ*, 133, 2892
- Melnick J., 1977, *ApJ*, 213, 15
- Melnick J., Terlevich R., Moles M., 1988, *MNRAS*, 235, 297
- Melnick J., Tenorio-Tagle G., Terlevich R., 1999, *MNRAS*, 302, 677
- Muñoz-Tuñón C., Tenorio-Tagle G., Castaneda H. O., Terlevich R., 1996, *AJ*, 112, 1636
- Mühle S., Klein U., Wilcots E. M., Hüttemeister S., 2005, *AJ*, 130, 524
- Oke J. B., 1990, *AJ*, 99, 1621
- Origlia L., Leitherer C., Aloisi A., Greggio L., Tosi M., 2001, *AJ*, 122, 815
- Osterbrock D. E., 1989, *Astrophysics of Gaseous Nebulae and Active Galactic Nuclei*. University Science Books, Mill Valley, CA
- Pittard J. M., 2007, in Hartquist T. W., Pittard J. M., Falle S. A. E. G., eds, *Astrophysics & Space Science Proc., Diffuse Matter from Star Forming Regions to Active Galaxies - A Volume Honouring John Dyson*. Springer, Dordrecht
- Pittard J. M., Dyson J. E., Falle S. A. E. G., Hartquist T. W., 2005, *MNRAS*, 361, 1077
- Reakes M., 1980, *MNRAS*, 192, 297
- Relaño M., Lisenfeld U., Vilchez J. M., Battaner E., 2006, *A&A*, 452, 413
- Roy J.-R., Aube M., McCall M. L., Dufour R. J., 1992, *ApJ*, 386, 498
- Sánchez S. F., 2004, *Astron. Nachr.*, 325, 167
- Scalo J. M., 1987, in Hollenbach D. J., Thronson H. A., Jr, eds, *ASSL Vol. 134, Theoretical Approaches to Interstellar Turbulence, Interstellar Processes*. D. Reidel Publ. Co., Dordrecht, p. 349
- Shopbell P. L., Bland-Hawthorn J., 1998, *ApJ*, 493, 129
- Sidoli F., Smith L. J., Crowther P. A., 2006, *MNRAS*, 370, 799
- Sirianni M. et al., 2005, *PASP*, 117, 1049
- Slavin J. D., Shull J. M., Begelman M. C., 1993, *ApJ*, 407, 83
- Stil J. M., Israel F. P., 1998, *A&A*, 337, 64
- Stil J. M., Israel F. P., 2002, *A&A*, 392, 473
- Storey P. J., Hummer D. G., 1995, *MNRAS*, 272, 41
- Suchkov A. A., Berman V. G., Heckman T. M., Balsara D. S., 1996, *ApJ*, 463, 528
- Taylor C. L., Hüttemeister S., Klein U., Greve A., 1999, *A&A*, 349, 424
- Tenorio-Tagle G., Muñoz-Tuñón C., Cox D. P., 1993, *ApJ*, 418, 767
- Tenorio-Tagle G., Muñoz-Tuñón C., Cid-Fernandes R., 1996, *ApJ*, 456, 264
- Tenorio-Tagle G., Muñoz-Tuñón C., Pérez E., Silich S., Telles E., 2006, *ApJ*, 643, 186
- Terlevich R., Melnick J., 1981, *MNRAS*, 195, 839
- Tokura D. et al., 2006, *ApJ*, 648, 355
- Tomita A., Ohta K., Saito M., 1994, *PASJ*, 46, 335
- Vacca W. D., Conti P. S., 1992, *ApJ*, 401, 543
- van Dokkum P. G., 2001, *PASP*, 113, 1420
- Veilleux S., Osterbrock D. E., 1987, *ApJS*, 63, 295
- Viallefond F., Allen R. J., Goss W. M., 1981, *A&A*, 104, 127
- Waller W. H., 1991, *ApJ*, 370, 144
- Westmoquette M. S., Smith L. J., Gallagher J. S., III, Exter K. M. 2007a, *MNRAS*, in press (doi:10.1111/j.1365-2966.2007.12252.x) (Paper II)
- Westmoquette M. S., Smith L. J., Gallagher J. S., III, O'Connell R. W., Rosario D. J., de Grijs R., 2007b, *ApJ*, in press
- Westmoquette M. S., Smith L. J., Gallagher J. S., III, 2007c, *MNRAS*, submitted (Paper III)
- Yang H., Chu Y.-H., Skillman E. D., Terlevich R., 1996, *AJ*, 112, 146

This paper has been typeset from a \LaTeX file prepared by the author.